CAAP Final Report

Date of Report: November 1, 2023
Revised Date: December 11, 2023

Prepared for: *U.S. DOT Pipeline and Hazardous Materials Safety Administration*

Contract Number: 693JK31950003CAAP

Project Title: Fundamental Understanding of Pipeline Material Degradation under Interactive Threats of Dents and Corrosion

Prepared by: Iowa State University

Contact Information: Professor Ashraf Bastawros,
T.A.Wilson Professor of Engineering,
Department of Aerospace Engineering
2271 Howe Hall, Rm 1200
Ames, IA 50011-2271
Phone: 515-294-3039 Fax: 515-294-3262
Email: bastaw@iastate.edu

Reporting Period: 9/29/2019-9/30/2023

Project Title: Fundamental Understanding of Pipeline Material Degradation under Interactive Threats of Dents and Corrosion

Table of Contents

List of Figures Page

List of Tables Page

List of Acronyms

API RP	American Petroleum Institute Recommended Practices
ASTM	American Society for Testing and Materials
EIS	Electrochemical Impedance Spectroscopy
FIB	Focus Ion Beam
FOV	Field of View
GB	Grain Boundary
HCF	High Cyclic Fatigue
HMH	Huber-Von Mises-Hencky Yield Criterion
IGSCC	Intergranular Stress Corrosion Cracking
LCF	Low Cyclic Fatigue
OD	Outer Diameter
PHMSA	Pipeline And Hazardous Materials Safety Administration
RVE	Representative Volume Element
SCC	Stress Corrosion Cracking
SEM	Scanning Electron Microscopy
SMYS	Systematic Minimum Yield Strength
UMAT	User Material Subroutine

A.1 Executive Summary

This is the Final Report for work completed under U.S. Department of Transportation Pipeline and Hazardous Materials Safety Administration (PHMSA) under contract number 693JK31950003CAAP, titled "Fundamental Understanding of Pipeline Material Degradation under Interactive Threats of Dents and Corrosion." The project was implemented to enrich the knowledge base for evaluating interactive threats of external mechanical dents and secondary features, through integrated lab-scale experimental and numerical framework to characterize and better predict the remaining safe life and operating pressures, while projecting the needs for mitigation measures. Three main objectives have been accomplished thought this work:

a) Develop understanding of the role of residual stresses on the acceleration of initiation of stress corrosion cracking.

b) Develop a numerical framework that can combine the role of residual stresses and accumulated plastic strains arising from dents and gouges on the reliable service and fatigue life limits of the pipeline.

c) Show the damage accumulation under restraint and unrestraint conditions for dented pipeline, and their evolution with increasing dent depth/pipe diameter ratio.

The final report presents the activities completed to develop an understanding of the role of mechanical damage on accelerated stress corrosion cracking and the impact of those defects on the structural integrity of operating the pipelines. The impact of residual stress on the initiation of stress corrosion cracking is assessed on modern pipeline steel (X70). While we were planning also to examine X80 steel. However, we came to the conclusion that the identified trends would also be applicable to X80 pipeline, when considering scalability of their strength and toughness. Accordingly, all our tests were conducted on X70 pipeline-grade steel. Electro-chemical impedance spectroscopy (EIS) is also utilized to characterize the corrosion-induced product layer. The developed continuum numerical framework combines the plastic damage arising from dents and gouges with the accumulated elastic damage, which leads to delayed failure (under fluctuating pressure loading, i.e., fatigue). A slight modification of the planned work is the calibration of the elasto-plastic fatigue model on historical data for vintage (X52) and modern (X70) steel, rather than employing a partial data set from lab-scale experiment. The modeling framework is then utilized to predict the fatigue life of full-scale testing of realistic dents and gouges based on a previous PHMSA research project[1].

The project results were shared with subject matter experts for possible guidance on the revision of the Pipeline Safety Management System standard, API RP 1183 to help reduce risk and enhance safety management programs for pipeline operators. The experimentally calibrated computational framework is amenable for systematic examination of multi-threat analysis at structural scale.

[1] U.S. Department of Transportation Pipeline and Hazardous Materials Safety Administration "Full Scale Testing of Interactive Features for Improved Models (Agreement DTPH56-14-T-00002)." [33]

A.2. Next Step

This project provides an initial assessment of the role of residual stresses arising from gouges and dents on the fatigue life of oil and gas pipelines. The project also provides assessments of the role of stress corrosion cracking (SCC) on reducing the strength of the pipelines, and the subsequent influence on their service life. A calibrated and verified numerical framework was developed to assess and predict both the conditions that lead to immediate (burst under constant loading conditions) and/or delayed failure (under fluctuating pressure loading (fatigue)). This framework is amenable to providing a comprehensive understanding of the effects of multi-threats of external mechanical damage and environmental attacks on the mechanical performance of oil and gas pipelines. In particular, the framework is amenable to integrating the interactive threats of corrosion and dynamic loading, as highlighted in A.2.1 and A.2.2 below.

A.2.1 Extended lab-scale investigation of the effect of residual stresses and plastic strains on SCC

Performing a full-scale SCC-crack propagation under cyclic loading is a long endeavor to allow the electrochemical process to develop. Alternatively, an accelerated lab-scale testing is more attainable with pre-strained samples exposed to electrochemical corrosion. The developed accelerated testing framework is amenable to such a task for sorting out the level of dent and gouge-induced residual stresses and plastic strain on the initiation and propagation of stress corrosion cracking. This will provide realistic quantification for the correlation between the plastic strain state arising from a dent or a gouge while being exposed to a corrosive environment. Establishing the current state of the material is an enabling step in the variance reduction of integrity analysis.

A.2.2 Numerical Assessments for a Wide Range of Interactive Threats

Having developed a well-calibrated numerical model that combines the plastic damage due to individual events with elastically accumulated damage due to operational conditions provides an enabling tool to address a wide range of perceived risks in pipeline operations. These include:

a) Evaluating and analyzing various damage and gouge scenarios, with the capability to assess the remaining safe operating life is essential. A critical situation arises when externally induced damage leads to locally increased residual elastic stresses. If these residual stresses alter the mean of fluctuating stress amplitudes, the remaining safe operational life for the affected section of the pipeline will be significantly impacted.
b) Corrosion-induced wall thinning effects. The developed numerical framework will enable the prediction of a combined safe operational pressure range.
c) Assessment of geohazard impact on a pipeline and the effect of longitudinal strain. Detailed bending analysis could be carried out with the developed elastoplastic accumulated damage with the ability to predict burst scenarios, strain capacity, and remaining fatigue life.
d) Assessment of rehabilitation methods employing inner coatings and inner-liners to mitigate corrosion and erosion material loss.

A.3 Dissemination of the Results:

We have strived to disseminate the findings from the project to further the current state of knowledge pertaining to mechanical damage and SCC assessment and modeling to academia, industry, and standards development organization groups and industry. A summary of our activities is listed here:

1. Bastawros, A. -F., "Fundamental Understanding of Pipeline Material Degradation under Interactive Threats of Dents and Corrosion," Government and Industry Pipeline PHMSA R&D Forum, Washington DC, Oct 31-Nov. 1, 2023.
2. Amir Abdelmawla, Ashraf Bastawros, "Effect of Pre-Accumulated Plastic Strain on Stress Corrosion Cracking and Fatigue Life of Steels; Experiment and Modeling," International Conference on Fracture, Atlanta, Georgia, June 11 – 16, 2023.
3. A. Abdelmawla, K. Kulkarni and A.F. Bastawros, 2023, Effect of Pre-Accumulated Plastic Strain on Stress Corrosion Cracking and Fatigue Life of Steels; Experiment and Modeling, Conference Proceedings of the Society for Experimental Mechanics Series. Society for Experimental Mechanics Annual Conference and Exposition, Orlando, Florida, June 5 – 8, 2023, (in press).
4. Amir Abdelmawla, Ashraf Bastawros, "Fatigue Damage Model for Predicting the Effect of Pres-straining on the Remaining Fatigue Life of Ti-Alloys," The Fourth International Conference on Damage Mechanics, Baton Rouge, Louisiana, USA, MAY 15 - 18, 2023.
5. Bastawros, A. –F., (Invited talk). "Corrosion: Interaction between Electrochemistry and Mechanics," Society of Engineering Sciences Meeting, Texas A&M College Station, October 16-21, 2022.
6. Pratyush Mishra, Denizhan Yavas, Abdullah Alshehri, Pranav Shrotriya, Ashraf Bastawros, Kurt R Hebert, 2021, "Model of vacancy diffusion-assisted intergranular corrosion in low-alloy steel," Acta Materialia 220: 117348. https://doi.org/10.1016/j.actamat.2021.117348
7. Denizhan Yavas, Thanh Phan, Liming Xiong, Kurt R. Hebert, Ashraf F. Bastawros, 2020, "Mechanical degradation due to vacancies produced by grain boundary corrosion of steel," Acta Materialia 200, 471-480. https://doi.org/10.1016/j.actamat.2020.08.080
8. Bastawros, A. -F., "Fundamental Understanding of Pipeline Material Degradation under Interactive Threats of Dents and Corrosion," Government and Industry Pipeline R&D Forum, Washington DC, February 19-20, 2020.
9. Pratyush Mishra, Denizhan Yavas, Abdullah Ashehri, Ashraf Bastawros, Pranav Shrotriya, Kurt Heber "Mechanism for Propagation of Intergranular Corrosion in Pipeline Steel," 236th ECS Meeting, Atlanta GA Oct. 13-17, 2019.
10. Denizhan Yavas, Thanh Phan, Liming Xiong, Kurt Hebert, Ashraf Bastawros, 2019, "Atomistic study of grain boundary degradation under intergranular electrochemical attack," Society of Engineering Sciences Meeting, St Louis MO, October 13-15, 2019.

11. We held a kick-off meeting on Nov. 13, 2019, via WebEx, which was attended by the PIs, graduate students, and the program monitor. The project objectives, milestones, and deliverables were presented and discussed.

A.3.1 Student Education:

Several students from different levels were involved in this project. This includes 4 undergraduate students, 1 MSc student, 1 PhD student, and 1 post-doctoral fellow.

Undergraduate students	**Department**	**Role**	**Status**
Jessica Dwyer	Mechanical Engineering	Helped in running the electrochemical corrosion experiment	Graduated and joined Boston Scientific as a Supplier Quality Engineer
Kaiser Aguirre	Aerospace Engineering	Helped in running the electrochemical corrosion experiment	Graduated and joined the graduate school at Case Western Reserve University
Mehmet Sefer	Aerospace Engineering	Helped in running the electrochemical corrosion experiment	Senior undergraduate
Graduate students			
Kaustubh Kulkarni	Aerospace Engineering	Experimentally investigate the effect of pre-accumulated plastic strain on the corrosion rate.	Graduated with MSc and joined Freeport-McMoRan as a Mechanical Engineer
Amir Abdelmawla	Aerospace Engineering	Helped in the experimental investigation of the effect of pre-accumulated plastic strain on the corrosion rate. Developed a fatigue damage model for the effect of dent on the fatigue life.	5th year PhD student

Post-docs

Denizhan Yavas	Aerospace Engineering	Helped in the electrochemical impedance spectroscopy analysis of the corrosion product layer	Assistant professor, Lamar University, TX

B. Experimental Program

B.1 High Throughput Lab-Scale Interactive Threat Screening

An apparatus with in-situ stress application during the electrochemical corrosion was designed and built as shown in Fig. 1. The corrosion setup had a micro-cell and loading mechanism. The new setup was used to mimic the interactive role of applied stress (resulting from a local gouge or indent) on the IGSCC conditions with variable time and stress levels. Figure 1 shows the current version of the new setup. The setup consists of (1) the micro-cell, (2) the sample holder mounted on the horizontal rail, and (3) the vertical linear translation stage with the micrometer adjustment and load transducer. In order to maintain better contact between the micro-cell and the samples, a silicone rubber cap is attached at the bottom orifice of the micro-cell. The rubber cab can also provide variable corrosion area by altering the hole diameter. The experimental protocol includes:

a) Mounting the cantilever steel strip in the sample holder
b) Loading the sample at its free-end by the vertical translation stage. The level of deflection was adjusted to provide the desired bending stress level at the root of the beam.
c) Engaging the micro-electrochemical cell with the sample surface, near the fixed support.
d) Filling the micro-electrochemical cell with the electrolyte and starting the corrosion experiment under the applied constant deflection. The corresponding end-load is monitored by the load transducer attached to the vertical stage.

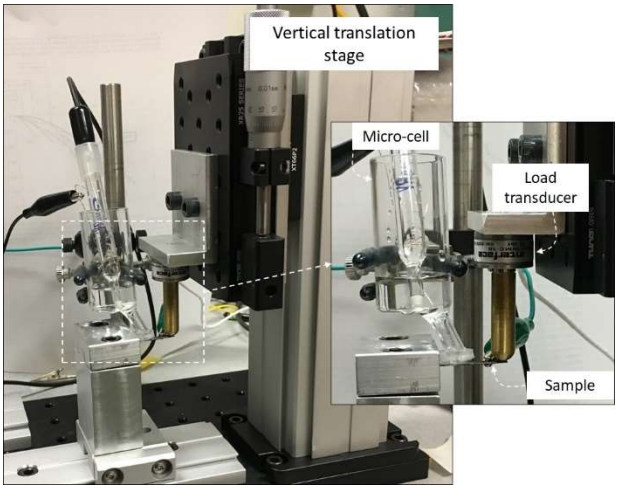

Figure 1: The micro-cell corrosion setup with the loading mechanism to mimic IGSCC conditions with variable stress levels.

B.2 Miniaturized Tensile Sample for Pre-accumulated Plastic Strain

In our initial study, we noticed that uniform cross-section tensile samples were failing within the tensile grips. To rectify this stress concentration effect, while utilizing a standard tensile sample configuration, we employed the numerically calibrated dog-bone miniaturized tensile sample configuration, shown in Fig. 2. The samples were machined in two directions: i) Direction parallel to the rolling direction ii) Direction transverse to the rolling direction. Tensile testing was conducted on a computer-controlled Instron (5960) frame with a displacement rate of 33.34 μm/s.

The test was conducted under strain control utilizing a noncontact video extensometer for automated strain recording and control of the strain rate. The utilized micro-tensile sample and the loading fixtures are shown in Fig. 2(c).

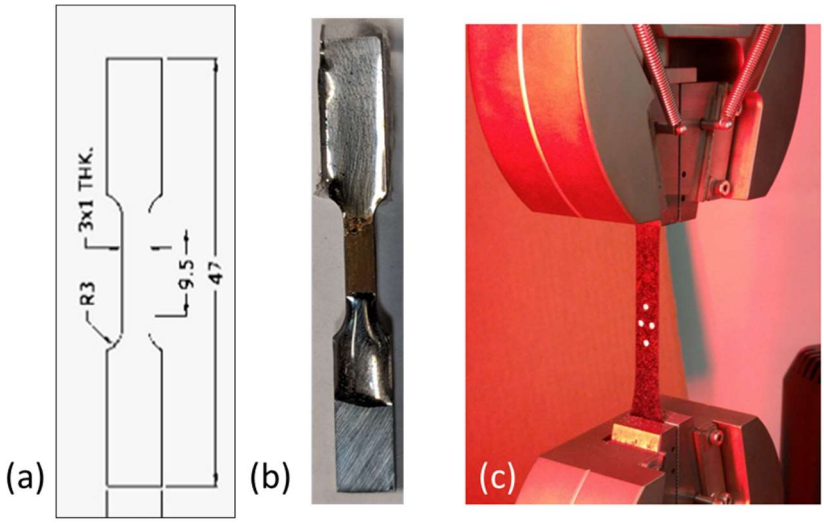

Figure 2: (a) dimensions of the miniaturized test samples. (b) Water-jet machined tensile corroded sample with a well-defined window for corrosion by epoxy coating. (c) The tensile sample with wasted cross-section was tested with a noncontact video extensometer for automated gauge-strain recording under the applied controlled strain rate.

Figure 3: The corrosion setup shows (a) a sample with reference and counter electrode and (b) completely insulated during the corrosion experiment. (1 M NaHCO3 solution with pH 8.1-8.2 and applied potential in the range of -0.4 to -0.6V).

The employed electrochemical cell for the corrosion experiment is shown in Fig. 3 for corrosion over the full gauge. The goal was to test the residual toughness of these samples after the initial application of plastic strains and corrosion, employing Charpy testing. However, further Charpy testing was not performed to allow for extensive surface analysis of the surface morphological features and grain boundary grooving. All corrosion experiments were carried out in a high-pH electrolyte solution of 1 M NaHCO3 with a pH in the range of 8.1-8.2 and an applied potential in

the range of -0.4 to -0.6V relative to Ag/AgCl. Tensile samples of X70 steel stock were machined with a length of 100 mm, a width of 5 mm, and a thickness of 1 mm. After applying the required pre-strain level, the corrosion samples were coated with an epoxy layer to define the corrosion window within the gauge length of the tensile sample, as shown in Fig. 2(b). Epoxy coating is proven to be a better replacement for lacquer coating as it does not degrade with long-term exposure (24 hours and 48 hours as well).

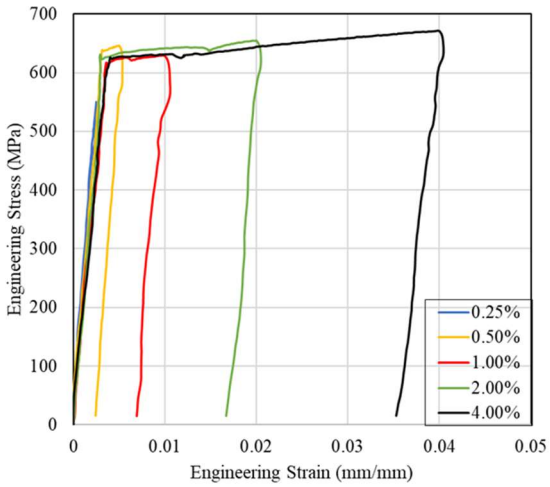

Figure 4: Tensile stress-strain results for predetermined strain levels of 0.25-4%, representing the residual plastic strain level within a shallow dent.

A set of tensile samples of X-70 pipeline steel was tested under displacement control to a predetermined engineering strain of 0.25, 0.5, 1, 2, and 4%. The chosen strain range represents a typical residual plastic strain level found within the dent shoulder and apex of a dented pipe. A summary of the recorded stress-strain curves for the examined set of samples is shown in Fig. 4. For the tested set, the stress-strain curves are remarkably repeatable with a well-identified yield stress of 600 MPa and a consistent level of post-yield hardening characteristics.

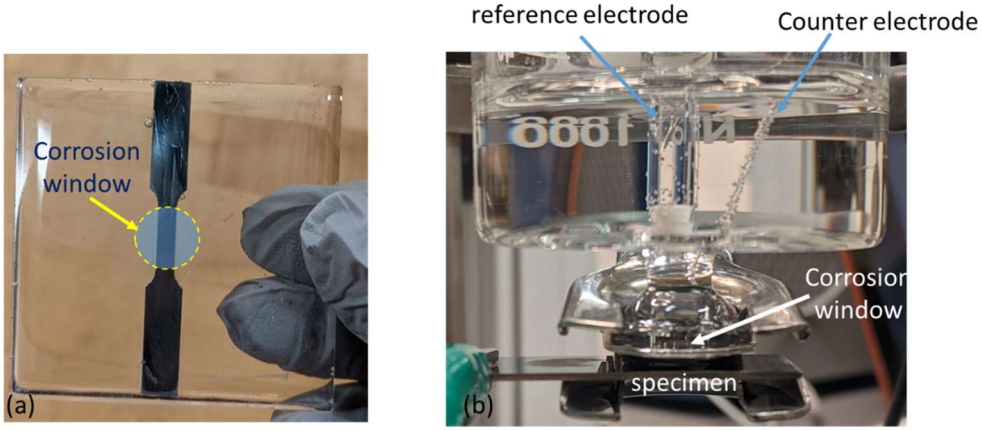

Figure 5: (a) Epoxy fixture to support the tensile sample underneath the electrochemical cell. The marked corrosion window is located within the uniform tensile strain range within the sample. (b) An electrochemical cell with an epoxy holder supports the sample for the electrochemical experiment.

A supporting epoxy holder was developed to support the sample under the electrochemical cell with a well-defined area for corrosion. The electrochemical cell exposure window was selected to induce corrosion within the uniform stress region of the sample, as shown in Fig. 5. The fixture provided the ability to expose the entire gauge length of the sample to the corrosion process, while retaining the ability to retest the sample again under tensile loading to failure. The generated sample sets that combines pre-straining and electrochemical exposure enabled us to examine our hypothesis that the increase of dislocation density due to residual plastic strain within the dent area will accelerate the corrosion rate. Moreover, the post-exposure tensile-tests helped to identify the total strain to failure after exposure, thereby setting the ductility limit of the material.

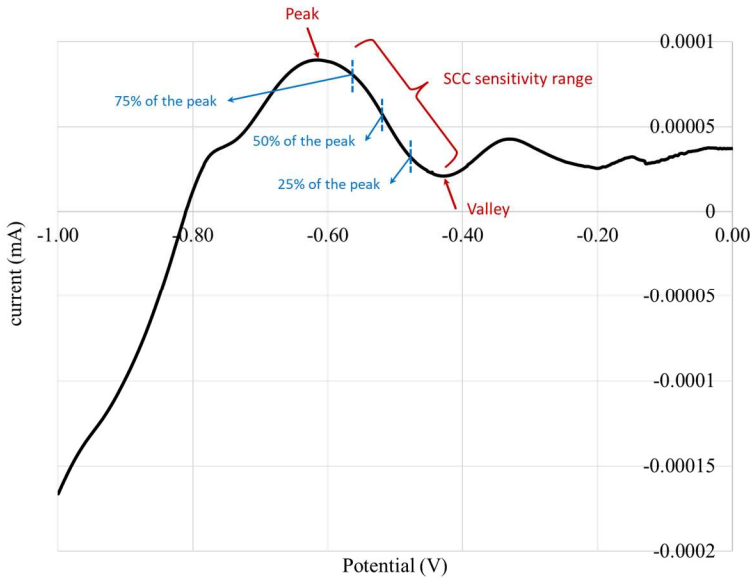

Figure 6: Current-voltage polarization curve to identify the SCC sensitivity range.

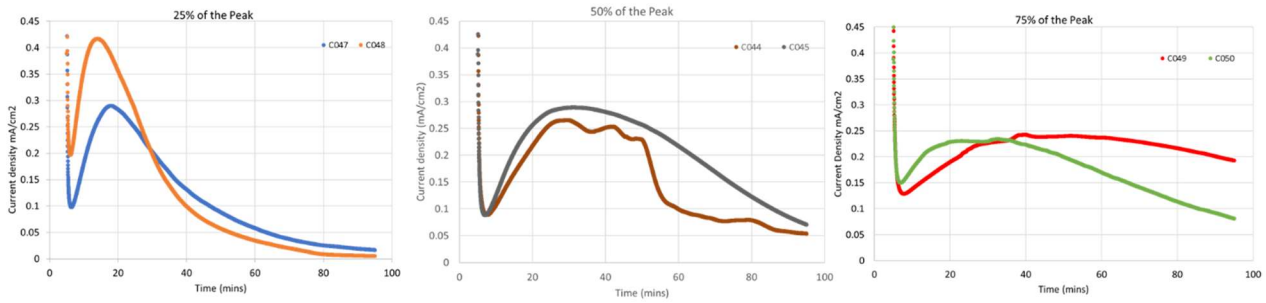

Figure 7: Current density-time traces for six different samples showing the peak current at different applied voltages, as measured by percentage from the peak traces. Legends in the figure refer to the designated samples numbers in Fig. 6.

All corrosion experiments were carried out in a high pH electrolyte solution of 1 M NaHCO3 with pH 8.1-8.2 and applied potential in the range of -0.4 to -0.6V relative to Ag/AgCl. First, we performed a repeatability study to narrow down the applied potential range for susceptibility to stress-corrosion cracking from the current-voltage sweep curve, shown in Fig. 6. This potential is

typically between the active dissolution peak of −0.60 V and the passivation potential of −0.40 V, noted on the current-voltage sweep curve in Fig. 6. We performed multiple repeatability tests for different applied voltage levels, which would induce about 25%, 50% and 70% of the peak current, noted in Fig. 6. This is identified as the distance between the peak and valley of the current within the range of -0.4 to -0.6V and then identify the percentage shift from the current peak. The multiple exposure results are shown in Fig. 7. We have identified the range from the peak to be the most sensitive domain for SSC and used shift resulting in 75% of the current peak to be used in all electrochemical testing.

B.3 Electrochemical Impedance Spectroscopy Analysis of Corrosion Product Layer

In the present study, electrochemical impedance spectroscopy (EIS) was used to investigate the evolution of electrochemical reactions and transport processes during the formation of a corrosion product layer on API X70 pipeline steel during high-pH corrosion in 1 M $NaHCO_3$ at active dissolution potentials. At these conditions, steel is susceptible to SCC. Our goal was to establish the EIS characteristics that might enable the usage as an NDE technique. The approach of exposure time-dependent EIS measurements is similar to that of Farelas et al. in their study of CO_2 corrosion [34]. Rather than analyzing EIS with equivalent circuit models as is typically done in the CO_2 corrosion literature, we derived the impedance response from a transient model of reactions and transport processes that explicitly incorporates key features of dissolution and passivation reactions, as outlined in our summary paper [35] and summarized in Fig. 8. The advantage of this approach is that it permits interpretation of parameters derived from model fitting in terms of the rate-controlling kinetic and transport processes. Thus, the present EIS results show that transient current decays are explained by the reduction of the effective diffusivity of carbonate anions through the corrosion product layer, which suppresses the primary dissolution reaction.

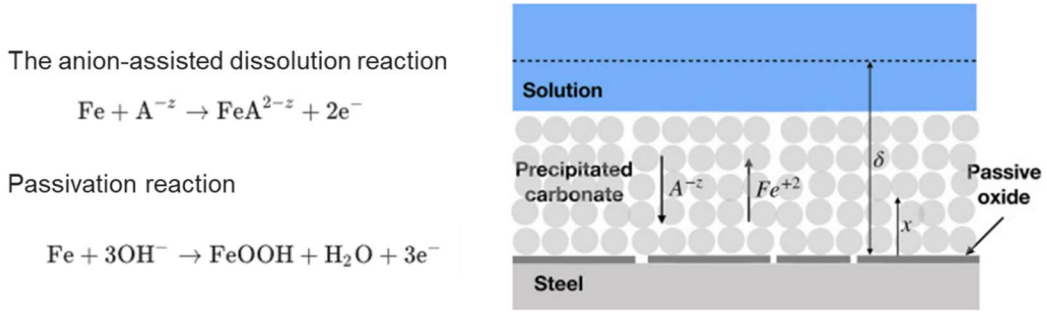

Figure 8: Schematic representation of model geometry. The corrosion product includes a thin passive oxide with partial coverage θ and a precipitated porous carbonate corrosion product layer. The acceptor anion A^{-z} may be either a carbonate or bicarbonate ion. Depending on the relative magnitudes of the diffusion resistances of the carbonate layer and external solution, the diffusion layer thickness δ may approximate the carbonate layer thickness or otherwise extend into the external solution, as shown.

The pipeline steel (API X70) composition in wt. % as measured by optical emission spectroscopy was 97.5 Fe, 0.095 C, 1.7 Mn and 0.37 Si. The ferrite phase was composed of equiaxed grains of about 5 μm width, with the minority pearlite phase forming elongated grains less than 5 μm wide.

Sample surfaces were polished to 600 grit finish, followed by cleaning with acetone and distilled-deionized water (resistivity 18 MΩ-cm). Experiments were carried out in a three-electrode cell similar to the configuration in Fig. 3 and 5, using a Potentiostat (Gamry Reference 3000), with the steel sample as the working electrode, platinum wire as the counter electrode, and an Ag/AgCl reference electrode. All potentials are measured with respect to this reference electrode. The corrosion test solution was naturally aerated 1 M $NaHCO_3$ (pH 8.1) at 25°C prepared with analytical grade reagents and distilled-deionized water. During a 2.5 h corrosion experiment, the solution pH increased to about 8.4 from its initial value, possibly due to CO_2 evaporation. Prior to the corrosion exposures, the steel surface was cathodically polarized at −1.0 V for 5 min to remove native oxide. Cathodic polarization was followed immediately by either linear potential sweeps or constant potential corrosion exposures at −0.521 V. This potential is between the active dissolution peak of −0.60 V and the passivation potential of −0.40 V and hence lies within the range of susceptibility to SCC and the subsequent IGSCC. The collection of impedance spectra was initiated immediately at the end of the constant potential exposures for durations between 5 min and 20 h. EIS acquisition was accomplished by superimposing a 10 mV RMS amplitude AC excitation on the applied potential and sweeping the AC frequency from 100 kHz to 0.1 Hz. Kramers-Kronig tests were performed using Gamry Echem Analyst software to validate the system stability over the frequency range. The corrosion product layer was examined by scanning electron microscopy (SEM, FEI Quanta 250).

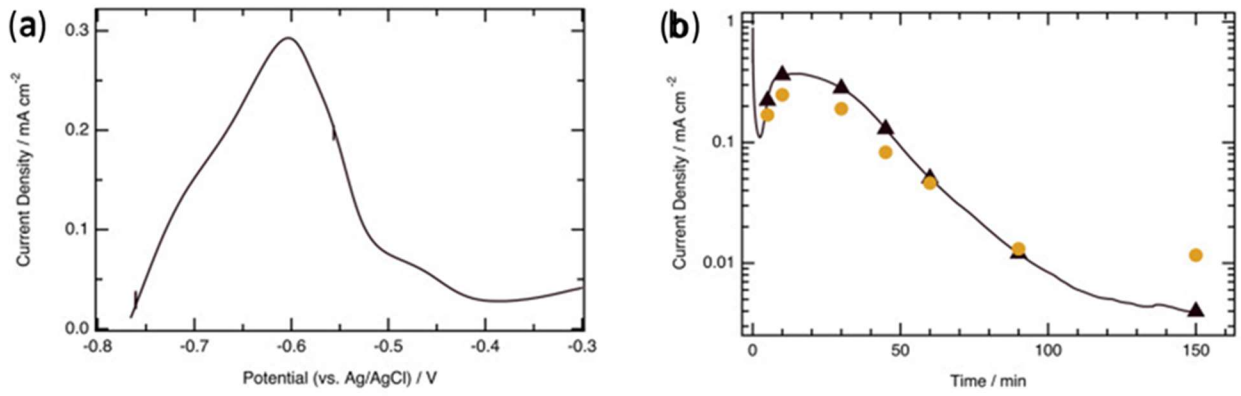

Figure 9: Electrochemical corrosion response of X70 steel in 1 M $NaHCO_3$ solution. (a) Potentiodynamic scan from −0.8 V to −0.2 V at 1 mV/s. (b) Current transient at −0.521 V. Triangular markers denote times at which impedance spectra were collected; circular markers are calculated by model based on kinetic parameters along with values of φ and $\overline{\theta}$ from the fitting of EIS.

Figure 9(a) shows an example of a potentiodynamic current-potential scan in 1 M $NaHCO_3$ at an intermediate potential for SCC susceptibility of -0.521V. Figure 9(b) shows a typical current transient at this potential. The current decayed to a minimum within 3 min, then increased to a maximum at around 10–20 min, and subsequently slowly decayed to values below 10 μA/cm^2 at 2.5 h. Cathodic current due to dissolved oxygen reduction may be significant relative to the corrosion current at long times when the measured current density is very small. In this case, the true corrosion current density would be somewhat larger than the recorded value.

B.4 Numerical Framework

The conceptual implementation of the interactive threats relies on an energetic/entropic based approach of the interactive failure process. The developed entropic viewpoint allows damage accumulation from all sources, including initial plastic damage, elasto-plastic fatigue damage, and while not being rigorously implemented, the influence of accelerated corrosion induced fatigue damage. Here, the basics of the elasto-plastic cumulative fatigue damage are highlighted, with their implementations to assess the fatigue life of dented pipes with restraint and unrestraint conditions.

B.4.1 Damage-coupled constitutive equations

Metals experience damage through the formation and propagation of micro-voids and micro-cracks within their microstructure. The degradation of these materials can be quantified using a damage variable within the framework of continuum damage mechanics. The mechanical behavior of a continuous medium can be described using a representative volume element (RVE), where all properties are represented by homogenized variables. As proposed by Lemaitre and Chaboche [1], in the case of isotropic materials, the damage variable, denoted as D, is employed to characterize the stiffness degradation of the RVE, which can be expressed as follows:

$$D = \frac{E - E_D}{E} \tag{1}$$

where E is the Youngs modulus of the material, E_D is the effective Youngs modulus of the RVE with damage, which ranges from E to 0, and consequently, the D value ranges from 0 to 1.

In fatigue damage, it is assumed that the damage can be represented by the decrease of material stiffness after each cycle. In the high cyclic fatigue (HCF) scenarios, the stress levels that the material is subjected to are typically lower than the yield stress. However, as the damage increases, the material may yield due to the increase of the effective stresses. Consequently, the damage evolution model should be coupled to an elastoplastic constitutive material model to simulate the mechanical response of a material subjected to fatigue damage. The classical theory of plasticity utilizes the Huber-von Mises-Hencky (HMH) yield criterion, which is commonly used to predict the mechanical behavior of metals [3]. In small strain formulation, the constitutive relation can be used along with the isotropic, kinematic, or combined hardening rules to describe the plastic behavior of metals under different loading conditions [4]. The simple kinematic hardening formulation proposed by Prager [5] is commonly adopted to solve different elastoplastic boundary value problems [6 – 7]. However, under complex loading scenarios such as cyclic loading, where the Bauschinger effect is observed, more advanced constitutive relations are needed to accurately describe the plastic response of materials. Armstrong and Frederick [8] developed an elastoplastic constitutive model to describe the evolution of the backstress resulting from reverse loading, which provides an accurate description of the cyclic plasticity response of metals. The proposed model was further developed by Chaboche and Rousselier [9] by integrating the isotropic hardening behavior rule towards constructing a combined hardening constitutive relation. In this hardening model, the isotropic rule proposed by Voce [10] was used by Chaboche and Rousselier [9] to

estimate the size of the yield surface. In addition, in the Armstrong–Frederick [8] model, it is assumed that the total back stress is a sum of several components. Therefore, the material behavior under high or low cyclic fatigue loadings can be simulated. As such, the damage-coupled elasto-plastic model is described in this section.

Under small deformation conditions, the total strain tensor, ϵ_{ij}, can be additively decomposed into elastic strain tensors, ϵ_{ij}^{e}, and plastic strain tensor, ϵ_{ij}^{p} as follow.

$$\epsilon_{ij} = \epsilon_{ij}^{e} + \epsilon_{ij}^{p} \tag{2}$$

In the damage-coupled constitutive framework, the damage is integrated with the constitutive equations using the concept of effective stress, which is the stress in the damaged area [2]. Therefore, the damage-coupled elastic strain is defined as

$$\epsilon_{ij}^{e} = \frac{1+\nu}{E}\sigma_{ij}^{D} - \frac{\nu}{E}\sigma_{kk}^{D}\delta_{ij} \tag{3}$$

where $\sigma_{ij}^{D} = \sigma_{ij}/(1-D)$ is the stress in the damaged area [2], σ_{ij} is the stress tensor, and ν is the Poisson's ratio.

In this work, the combined isotropic-nonlinear-kinematic hardening model proposed by Chaboche [1, 9, 11] is adopted along with the von Mises yield criterion such that the yield function can be expressed as

$$f_y = \sigma_{eq}^{D} - R\left(\overline{\epsilon}_p\right) - \sigma_y \tag{4}$$

$$\sigma_{eq}^{D} = \sqrt{(3/2)\left(S_{ij} - X_{ij}\right)\left(S_{ij} - X_{ij}\right)} \tag{5}$$

where $R\left(\overline{\epsilon}_p\right)$ is the isotropic hardening function, which represents the expansion or the reduction in size of the yield function, $\overline{\epsilon}_p$ is the equivalent plastic strain, σ_y is the yield strength of the material, X_{ij} is the shift or the back stress tensor, as shown in Fig. 10, and $S_{ij} = \sigma_{ij}^{D} - (\sigma_{kk}^{D}/3)\delta_{ij}$, which is the deviatoric part of the effective stress tensor

Fig. 10 presents a schematic illustration for the yield surface evolution under the combined hardening model. As it can be depicted form the figure, the material yields when $f_y > 0$. The evolution of the plastic strain rate is defined according to the associated flow rule, as shown in Fig. 10 as follows.

$$\dot{\epsilon}_{ij}^{p} = \dot{\lambda}\left(\frac{\partial f_y}{\partial \sigma_{ij}}\right) \tag{6}$$

where $\dot{\lambda}$ is the plastic multiplier.

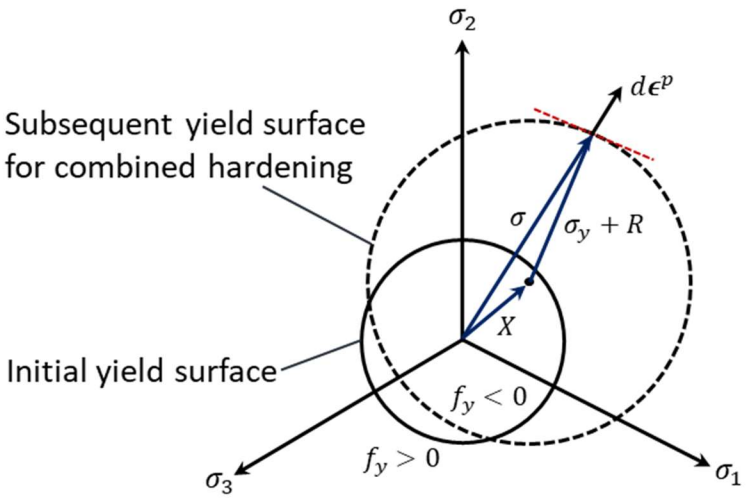

Figure 10: Schematic representation of the evolution of the yield surface under the combined hardening model.

Then, from the consistency condition, the evolution of plastic strain increment can be obtained as follows [4]

$$d\epsilon_{ij}^{p} = \frac{3}{2}\left(\frac{d\overline{\epsilon}_p}{1-D}\right)\overline{n} \tag{7}$$

where $d\overline{\epsilon}_p$ is the increment of the accumulated plastic strain, $\overline{n} = \left(S_{ij} - X_{ij}\right)/\sigma_{eq}^{D}$, which is the normalized effective stress tensor.

The combined isotropic and kinematic, with two back stress components, hardening model governed by Voce law [10] and Armstrong–Frederick [8] is adopted to update the size of the yield surface and the shift tensor, respectively [2, 4] such that.

$$R\left(\overline{\epsilon}_p\right) = Q\left(1 - e^{-b\overline{\epsilon}_p}\right) \tag{8}$$

where Q and b are material parameters representing the maximum increase in the yield surface (peak stress) and the rate of the stabilization, respectively.

The total back-stress tensor, X_{ij}, is assumed to be a sum of two components such that $X_{ij} = (1-D)\sum_{k=1}^{2} X_{ij}^{k}$ where each component is incrementally evolve according to Armstrong–Frederick relation [8] as follow.

$$dX_{ij}^{k} = \frac{2}{3}C_k d\epsilon_{ij}^{p} - \gamma_k d\overline{\epsilon}_p X_{ij}^{k} \tag{9}$$

where C_k, and γ_k, are material parameters responsible for strain hardening and dynamic recovery, respectively. In uniaxial case, C/γ is equal to the saturated, steady-state value of the back stress, and γ is the rate of saturation [4].

Since the back-stress components are incrementally evolving such that $X_{ij}^k = X_{ij}^k\big|_o + dX_{ij}^k$, where $X_{ij}^k\big|_o$, is the back stress from the previous step; the components of back stress can also be rewritten as follows

$$X_{ij}^k = \omega_k \left(X_{ij}^k\big|_o + \frac{2}{3} C_k d\epsilon_{ij}^p \right) \tag{10}$$

where $\omega_k = 1/\left(1 + \gamma_k d\overline{\epsilon}_p\right)$

When the material yields, the plastic strain increment is obtained by solving the following equation.

$$\left(\sigma_y + R\left(\overline{\epsilon}_p\right)\right) \xi\left(d\overline{\epsilon}_p\right) - J_2\left(Z_{ij}\right) = 0 \tag{11}$$

where $\xi\left(d\overline{\epsilon}_p\right)$ is a function of the equivalent plastic and is written as follows.

$$\xi\left(d\overline{\epsilon}_p\right) = 1 + \left(3\mu + \sum_{k=1}^{2} \omega_k C_k \right) \frac{d\overline{\epsilon}_p}{\sigma_y + R\left(\overline{\epsilon}_p\right)} \tag{12}$$

And the stress tensor, Z_{ij}, takes the following form.

$$Z_{ij} = S_{ij} - \sum_{k=1}^{2} \omega_k X_{ij}^k \tag{13}$$

and $J_2\left(Z_{ij}\right) = \sqrt{(3/2) Z_{ij} \cdot Z_{ij}}$.

The Newton–Raphson method approach is used to numerically solve Eq. (11) towards obtaining the equivalent plastic strain increment. To illustrate, first, let us call Eq. (11) to be $r\left(d\overline{\epsilon}_p\right)$ such that,

$$r\left(d\overline{\epsilon}_p\right) = \left(\sigma_y + R\left(\overline{\epsilon}_p + d\overline{\epsilon}_p\right)\right) \xi\left(d\overline{\epsilon}_p\right) - J_2\left(Z_{ij}\right) = 0. \tag{14}$$

The equivalent plastic strain increment is then obtained as follows.

$$d\overline{\epsilon}_p = d\overline{\epsilon}_p^o - \left. \frac{r\left(d\overline{\epsilon}_p\right)}{\partial r\left(d\overline{\epsilon}_p\right)/\partial d\overline{\epsilon}_p} \right|_{d\overline{\epsilon}_p = d\overline{\epsilon}_p^o} \tag{15}$$

where $d\overline{\epsilon}_p^o$ is the equivalent plastic strain increment from the previous step, and the first derivative of the $r\left(d\overline{\epsilon}_p\right)$ function, $\partial r\left(d\overline{\epsilon}_p\right)/\partial d\overline{\epsilon}_p$, is obtained as follows.

$$\frac{\partial r(d\bar{\epsilon}_p)}{\partial d\bar{\epsilon}_p} = \frac{\partial R(\bar{\epsilon}_p)}{\partial d\bar{\epsilon}_p}\,\xi(d\bar{\epsilon}_p) + \left(\sigma_y + R(\bar{\epsilon}_p + d\bar{\epsilon}_p)\right)\frac{\partial \xi(d\bar{\epsilon}_p)}{\partial d\bar{\epsilon}_p} - \frac{\partial J_2(Z_{ij})}{\partial d\bar{\epsilon}_p} \tag{16}$$

Where the individual derivatives are as follows

$$\frac{\partial R(\bar{\epsilon}_p)}{\partial d\bar{\epsilon}_p} = \frac{\partial R(\bar{\epsilon}_p)}{\partial \bar{\epsilon}_p}\frac{\partial \bar{\epsilon}_p}{\partial d\bar{\epsilon}_p} = \frac{dR(\bar{\epsilon}_p)}{d\bar{\epsilon}_p} = Qbe^{-b\bar{\epsilon}_p} \tag{17}$$

$$\frac{\partial \xi(d\bar{\epsilon}_p)}{\partial d\bar{\epsilon}_p} = \frac{1}{\sigma_y + R(\bar{\epsilon}_p)}\left[3\mu + \sum_{k=1}^{2}\omega_k C_k\left(1 - \gamma_k\omega_k d\bar{\epsilon}_p\right) + \left(1 - \xi(d\bar{\epsilon}_p)\right)\frac{dR(\bar{\epsilon}_p)}{dd\bar{\epsilon}_p}\right] \tag{18}$$

$$\frac{\partial J_2(Z_{ij})}{\partial d\bar{\epsilon}_p} = \frac{3}{2}\sum_{k=1}^{2}\gamma_k\omega_k^2\left(\bar{n}\cdot X_{ij}^k\right) \tag{19}$$

In the implementation of the elastoplastic constitutive model, the radial return mapping algorithm is used to obtain the equivalent plastic strain and update plastic strain and effective stress tensors. The solution process starts by obtaining the stress predictor for the current increment using Eq. (3). Then, the Von-Mises effective stress is calculated to check if the material yields according to Eq. (4). If $\sigma_{eq}^D < R(\bar{\epsilon}_p) + \sigma_y$ then the material response is still elastic. In such a case, the plastic strain and the back stress tensors will be updated to be the same as the previous step. If $\sigma_{eq}^D > R(\bar{\epsilon}_p) + \sigma_y$ then the material response is plastic. In this case, we use the equivalent plastic strain increment and the back stress tensors from the previous step to obtain the derivatives Eq. (16) - Eq. (19). Afterward, the new equivalent plastic strain increment is obtained from Eq. (15) and then used to update the back stress tensors according to Eq. (10), plastic strain tensor according to Eq. (7), and the corrector stress, according to Eq. (20) as follows,

$$S_{ij} = X_{ij} + \frac{Z_{ij}}{\xi(d\bar{\epsilon}_p)} + (\sigma_{kk}^D/3)\delta_{ij}. \tag{20}$$

Finally, the elastoplastic stiffness matrix is updated using Eq. (21) as follows,

$$C^{e-p} = \lambda^*\mathrm{I}\otimes\mathrm{I} + 2\mu^*\mathrm{I} + \frac{h^*}{1+h^*/3\mu^*}\bar{n}\otimes\bar{n} - \frac{1-\mu^*/\mu}{1+h^*/3\mu^*}\sum_{k=1}^{2}\gamma_k\omega_k^2\left[X_{ij}^k\otimes\bar{n} - \frac{3}{2}(\bar{n}\cdot X_{ij}^k)\bar{n}\otimes\bar{n}\right]. \tag{21}$$

The effective hardening modulus, effective Lamé constant, and the effective shear modulus are calculated using Eq. (22), Eq. (23), and Eq. (24), respectively, as follows,

$$h^* = \sum_{k=1}^{2}\omega_k C_k\left(1 - \gamma_k\omega_k d\bar{\epsilon}_p\right) + \frac{dR(\bar{\epsilon}_p)}{d\bar{\epsilon}_p} - \frac{\partial J_2(Z_{ij})}{\partial d\bar{\epsilon}_p}, \tag{22}$$

$$\lambda^* = K - \frac{2}{3}\mu^*, \tag{23}$$

$$\mu^* = \mu\left(1 - \frac{3\mu\, d\bar{\epsilon}_p}{J_2(Z_{ij})}\right). \tag{24}$$

In Eq. (23), $K = E/3(1-2\nu)$, which is the bulk modulus, $\mu = E/2(1+\nu)$, which is the shear modulus.

A detailed derivation of Eq. (11), Eq. (16) - Eq. (19), and the updated elastoplastic stiffness matrix is illustrated in great detail by Suchocki in [12]. Finally, the elastoplastic model is implemented into FE through a UMAT subroutine.

B.4.2 Fatigue damage model

In high-cyclic fatigue, plastic deformations may occur in stress concentrator zones such as notches or due to the increase of stress levels above yielding. For the case of pipeline gouges and dents, plastic deformation is already accumulated at these sections. A model that combine initial plastic damage with the evolving damage of the cyclic loading is developed. The combined model is an additive of the elastic and plastic fatigue damage, such that the total material damage can be decomposed into two parts.

$$D = D^e + D^p \tag{25}$$

where D^e and D^p are the elastic and plastic damage parameters, respectively.

In Eq. (25), the elastic damage is governed by the state of the cyclic stress, and the plastic damage is governed by the accumulated plastic strain over each loading cycle [14]. Moreover, in Eq. (25), there are three different cases to be considered. The first case is where the elastic deformation is dominant (e.g., high cyclic fatigue), and the total damage of the material involves only the elastic damage part. The second case is where the plastic deformation is dominant and elastic damage is negligible (e.g., low cyclic fatigue), and the total damage of the material involves only the plastic damage part. The last case is where elastic and plastic damage are equivalent, such that the total damage must be additively combined [14]. The damage evolution equation for the two cases will be presented in the following section.

(a) Elastic damage model

The cumulative damage fatigue model developed by LeMaitre and Chaboche [14] is one of the most commonly used models for fatigue damage. In this model, the damage is calculated based on the state of the stress at a material point. LeMaitre and Chaboche proposed the form shown in Eq. (26) for the accumulation of damage per cycle with an ultimate purpose of fitting the Woehler fatigue curve (S-N curve) of a particular material subjected to uniaxial fatigue loading.

$$\frac{dD^e}{dN} = \frac{\sigma_{max} - \sigma_l(\overline{\sigma})}{\sigma_u - \sigma_{max}}\left(\frac{\sigma_{max} - \overline{\sigma}}{M_o(\overline{\sigma})}\right)^{\beta} \tag{26}$$

where N is the number of cycles to failure, σ_{max} is the maximum applied stress within the loading cycle, $\overline{\sigma}$ is the mean stress for the uniaxial loading, within the loading cycle, β is a material constant, and the function $M_o(\overline{\sigma})$ is used to quantify the effect of mean stress and is given as:

$$M_o(\overline{\sigma}) = M_o(1 - b_2\overline{\sigma}) \tag{27}$$

where M_o and b_2 are material constants determined from fatigue tests, which have dimensions of MPa and MPa^{-1}, respectively.

The fatigue limit function $\sigma_l(\overline{\sigma})$ depends on the mean stress according to Goodman's relation, which is written as follows.

$$\sigma_l(\overline{\sigma}) = \sigma_{lo} + \overline{\sigma}(1 - b_1\sigma_{lo}) \tag{28}$$

where σ_{lo} is the fatigue limit at the fully reversed loading condition and b_1 is a characteristic material constant, which should be of order $(1/\sigma_u)$ MPa^{-1} [1].

As illustrated in [1], Eq. (26) does not provide a nonlinear accumulation of fatigue damage over time (cycles). This is because the loading and damage variables are separable. This formulation may work when there are variations in the amplitude and mean values of applied cyclic loads [1]. Consequently, to account for nonlinear accumulation (i.e., for different stress levels, mean and amplitude values), a more advanced damage evolution formula with a coupling between load parameters and D should be introduced [1] such that:

$$\frac{dD^e}{dN} = \left[1 - (1 - D)^{\beta+1}\right]^{\alpha} \left[\frac{\sigma_{max} - \overline{\sigma}}{M_o(1 - b_2\overline{\sigma})(1 - D)}\right]^{\beta} \tag{29}$$

Nevertheless, the multiaxial nature of loads in real engineering applications necessitates a further extension of the fatigue damage model to the 3D space to be given in the following form:

$$\frac{dD^e}{dN} = \left[1 - (1 - D)^{\beta+1}\right]^{\alpha} \left[\frac{\tau_a}{M_o\left(1 - 3b_2\sigma^D_{H,mean}\right)(1 - D)}\right]^{\beta} \tag{30}$$

where τ_a is the amplitude of the octahedral shear stress, which is expressed by:

$$\tau_a = \frac{1}{2}\sqrt{\frac{3}{2}\Delta S_{ij} \cdot \Delta S_{ij}}\,. \tag{31}$$

Where $\Delta S_{ij} = S_{ij,max} - S_{ij,min}$, and $S_{ij,max}$ and $S_{ij,min}$ are the maximum and minimum values of the deviatoric stress tensor components during one loading cycle. The mean hydrostatic stress for multi-axial stress state, $\sigma^D_{H,mean}$, in Equ. (30) is defined by:

$$\sigma^D_{H,mean} = \frac{1}{2}[\sigma^D_{H,max} + \sigma^D_{H,min}] \tag{32}$$

where $\sigma^D_{H,max}$ and $\sigma^D_{H,min}$ are the maximum and minimum hydrostatic stresses during one loading cycle.

In Eq. (30), the function α describes the effect of cyclic loading on the evolution of damage. More preciously, it couples the damage with the applied load, which is given by:

$$\alpha = 1 - a\,\langle \frac{\tau_a - \tau_a^*}{\sigma_u - \sigma_{eq,max}^D} \rangle \tag{33}$$

where $\sigma_{eq,max}^D$ is the maximum Von-Mises stress during one loading cycle, σ_u is the ultimate tensile stress, a is a material parameter determined from fatigue tests, and the MacCaulay bracket for a variable x , where $\langle x \rangle = x$ if $x \geq 0$ and $\langle x \rangle = 0$ if $x < 0$. The Sines [15] fatigue limit criterion for multiaxial loading, τ_a^*, is given by:

$$\tau_a^* = \sigma_{lo}\left(1 - 3b_1\sigma_{H,mean}^D\right) \tag{34}$$

(b) <u>Plastic damage model</u>

Lemaitre [14] proposed a plastic deformation-induced damage evolution model for ductile material damage. This model is based on the irreversible energy dissipation during plastic deformation. In this model, the dissipation potential due to damage is written as follows,

$$\phi = \frac{S}{m+1}\left(-\frac{Y}{S}\right)^{m+1} \tag{35}$$

where Y is the release rate of the strain energy density, which is derived from the thermodynamic potential and written as follows [14],

$$-Y = \frac{\left(\sigma_{eq}^D\right)^2 R_v}{2E} \tag{36}$$

where R_v is the tri-axiality function, which takes this form,

$$R_v = 2(1+\nu)/3 + 3(1-2\nu)\left(\sigma_H^D/\sigma_{eq}^D\right)^2. \tag{37}$$

The damage evolution law is derived from Eq. (35) by differentiating with respect to Y, given as:

$$\dot{D} = \dot{\lambda}\frac{\partial \phi}{\partial Y} = \left(-\frac{Y}{S}\right)^m \bar{\epsilon}_p \tag{38}$$

Furthermore, the proposed model was further extended by Lemaitre and Desmorat [2] to calculate the incremental fatigue damage caused by the plastic strain accumulation for metals subjected to low cyclic fatigue loading. The damage accumulation over each cycle is calculated as follows:

$$\frac{dD^p}{dN}\int_{1\ cycle} \dot{D}\,dt = \left[\frac{\left(\sigma_{eq}^D\right)^2 R_v}{2ES}\right]^m \Delta\bar{\epsilon}_p \tag{39}$$

where S and m are the energetic damage parameter and the unified damage exponent, respectively, which are obtained from the full uniaxial tensile test (a complete test up to the final rapture). $\Delta\bar{\epsilon}_p$ is the accumulated plastic strain over the loading cycle.

The total incremental damage is then calculated as the summation of the elastic and plastic damage increments per cycle such that.

$$\frac{dD}{dN} = \frac{dD^e}{dN} + \frac{dD^p}{dN} \tag{40}$$

In the above equation, the damage becomes totally elastic damage when the deformation is within the elastic regime or totally plastic damage when the plastic strain is large. In this way, the damage evolution framework can be adopted to investigate the material behavior in both high-cycle and low-cycle fatigue scenarios. Furthermore, in the elastic damage model, six parameters are calibrated according to the experimental fatigue data. For example, constants a, b_1 , and b_2 are obtained from fatigue data at different loading ratios (e.g., $R = -1,\ 0, \text{and} -0.5$). The values of β and M_o are determined from fully reversed stress-life data.

(c) Coupled Solution Process

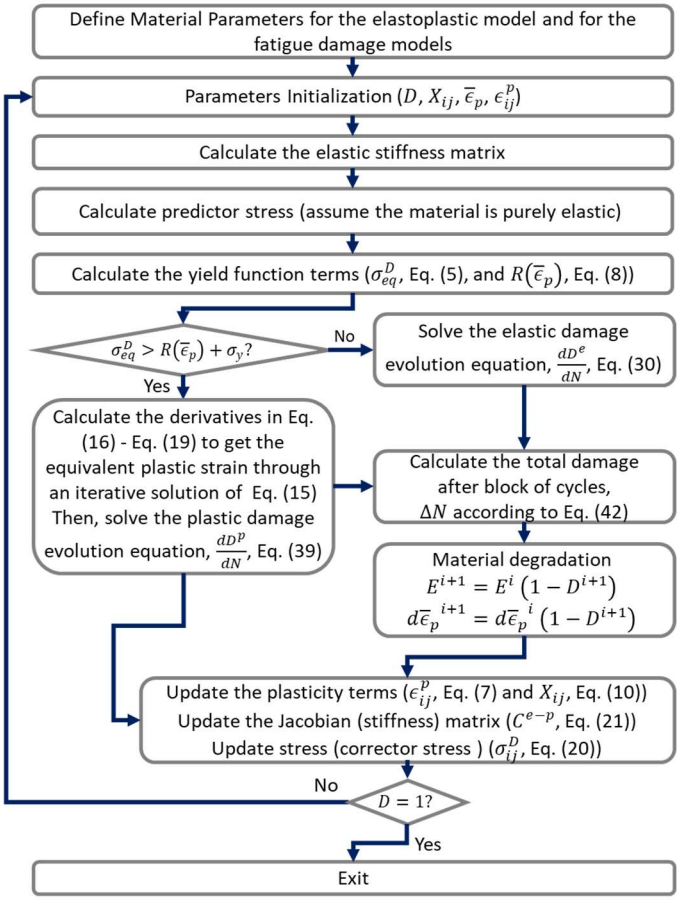

Figure 11: Flowchart of the solution process of the damage-coupled elastoplastic fatigue model

The solution process of the damage-coupled elastoplastic fatigue model is illustrated in a flowchart and presented in Fig. 11. The process starts by defining the material parameters and initializing the solution variables for the elastoplastic model and for the fatigue damage models. Then, the elastic stiffness matrix and the stress predictor for the current time increment are calculated from Hooke's law, assuming that the material is purely elastic at the beginning of the time increment. Afterward, the Von-Mises effective stress is calculated to check if the material yields according to Eq. (4). If the material response is still elastic, the elastic fatigue damage is computed by solving Eq. (30), and the plastic strain and the back stress tensors will be updated to be the same as the previous time increment. If the material yields the equivalent plastic strain increment and the back stress tensors from the previous step to obtain the derivatives Eq. (16) - Eq. (19) and the new equivalent plastic strain increment is obtained from Eq. (15) and then used to calculate the plastic damage evolution equation, Eq. (39). The total damage is computed and then used to estimate the amount of material degradation according to Eq. (42) and Eq. (41), respectively. Finally, the new equivalent plastic strain, along with the total damage, are used to update the back stress tensors according to Eq. (10), plastic strain tensor according to Eq. (7), and the corrector stress, according to Eq. (20), and the Jacobian matrix, according to Eq. (21), as described in Fig. 11.

C. Results and Discussion

C.1. Coupled Pre-accumulated Plastic Strain and Electrochemical Corrosion

This study elucidates the influence of external mechanical damage, such as dents or gouges, in inducing over-stressing, thereby reducing the threshold stress required for crack initiation below the average operating stress level. The primary objectives of this research are twofold: (i) to investigate the impact of initial corrosion on diminishing the residual strength of the pipeline, assessed in terms of strength and toughness, and (ii) to examine the influence of pre-stress on the initiation and advancement of the corrosion process, evaluated in terms of total corrosion charges, as well as the depth and morphology—including grooving and subsurface cracks—of the corroded surface.

C.1.1 Lab-scale investigation of corrosion-residual strength interactive threats

The focus of this set of experiments is to examine how initial exposure to corrosion might lower the residual strength of the pipeline (measured in terms of strength and toughness). For this set of tests, we utilized the electrochemical cell for the corrosion experiment, shown in Fig. 3. All corrosion experiments were carried out in a high pH electrolyte solution of 1 M $NaHCO_3$ with pH 8.1-8.2 and applied potential in the range of -0.4 to -0.6V relative to Ag/AgCl. Tensile samples of X70 steel stock were machined with a length of 100mm, width of 5mm, and thickness of 1mm. The corrosion samples were coated with a lacquer to define the corrosion window across the tensile sample gauge length. Figure 12 shows the sample preparation and testing steps. The original configuration of the tensile sample was defined with a window for corrosion, as shown in Fig. 12(a). The sample was then corroded for 24 hours under constant voltage, removed from the

solution, and dried. A cleaning step was followed to remove the defining lacquer coating so as not to interfere with the testing protocol. Subsequently, the corroded sample was tested under tensile loading to failure under a crosshead displacement control of 50μm/s. Four lacquer marks were deposited on the sample gauge-length to provide reference points for non-contact video extensometers. This allowed in situ monitoring of the axial and transverse strain components over the corroded sample gauge. Figure 12(c) shows the final failure gauge section with the marks indicated.

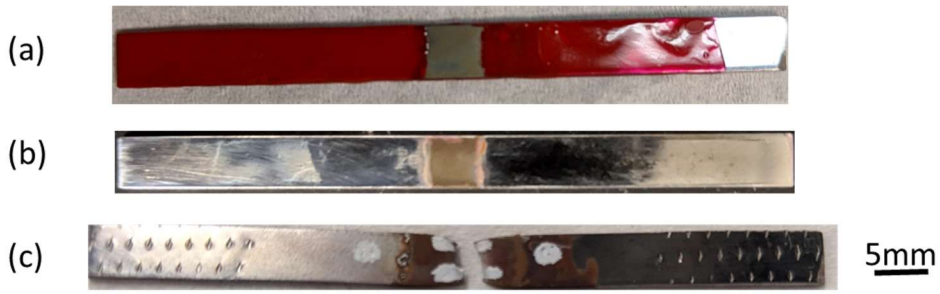

Fig. 12: Sequence of corrosion-tensile failure testing. (a) The defined corrosion window with lacquer coating. (b) Corroded sample with the corrosion region within the gauge length. (c) The final failure of the corroded sample after the tensile testing step. The white dotes are for in situ axial and transverse strain measurements.

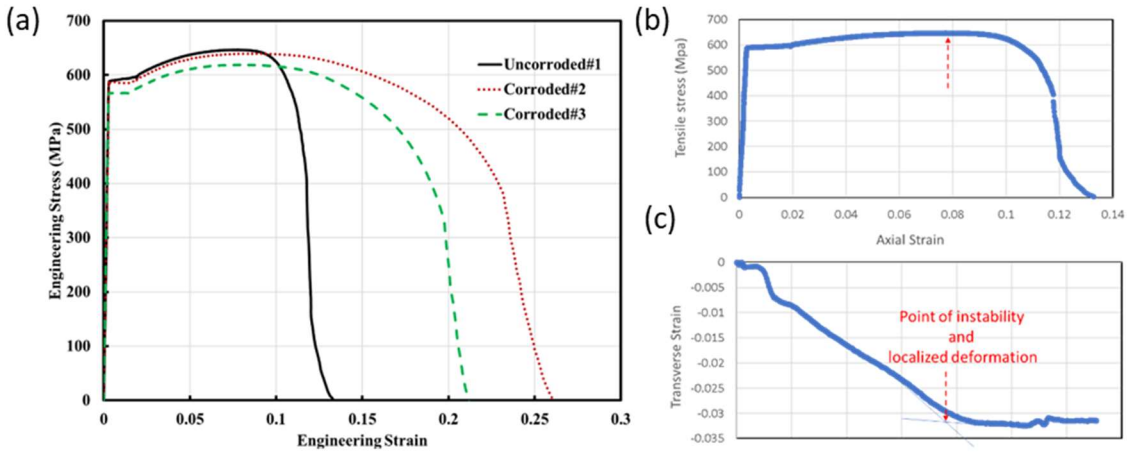

Fig. 13: (a) Comparison of the stress-strain curve for the corroded sample with the reference uncorroded sample. The initial results imply a reduction of the tensile yield strength, though unexpectedly, an increase in ductility may be identified. (b) stress-strain curve with ambiguous identification of the localized necking strain. (c) Utilization of axial vs. transverse strain distribution to identify the start of the localized necking.

A summary of the preliminary testing result of the remaining strength after corrosion is shown in Fig. 13(a), along with the strength of the version sample for comparison. It is clear that the initial yield strength of the corroded sample is statistically lower by about 10% in comparison with the

reference sample (the average of several tests showed variability of the yield strength of about ±2%). This is critical evidence of the effect of the corrosion on the yield strength of the pipeline steel. However, one might also conclude that the ductility limit, and thereby toughness, might have increased due to corrosion. However, the extent of deformation after the ultimate tensile strength is critically dependent on the geometry of the localization (cup and cone fracture), as well as the possibility of nucleation of cracking from the corrosion process.

Typically, toughness and, thereby, ductility are measured by the Charpy test. However, identifying the ductility or toughness from the curve is slightly ambiguous as the peak stress, as shown in Fig 13(b), may not correspond to the critical strain for homogeneous deformation before the localization process. Beyond the homogeneous deformation, the details of the stress-strain curves are a function of the details of the geometric details of localized deformation. However, in our measurements, we have another parameter, which is the transverse strain. The ratio between the transverse and axial strain is the Poisson's ratio for the incompressible homogeneous plastic flow, and is approximately =0.5. Figure 13(c) clearly shows the transition from macroscopic homogeneous deformation to localized necking on the axial vs transverse strain plot. Such a transition cannot be clearly identified on the stress-strain curve of Fig. 13(b). Having these issues, we decided to preserve the initially strained and corroded samples for further surface analysis in order to quantitatively assess the morphological evolution of the corrosion products. Additional repeatability study was required to generate the samples for Charpy test. However, employing results from full test fatigue data [24, 33] in model calibration (Section B4) alleviated the requirements of executing such a repeatability study for Charpy testing.

This set of experiments showed that initial exposure to corrosion has a statistically insignificant effect on lowering the residual strength or toughness of the base pipeline materials. The initial effect of corrosion appears to be primarily geometrical, resulting in spatial material loss at the site of corrosion. Such localized reduction of the wall thickness and the associated spatial topographical details might lead to; (i) reduction of burst pressure and (ii) sites with increase stress concentrations that accentuate the nucleation and propagation of fatigue cracks.

C.1.2 Role of Pre-accumulation of Plastic Strain on Corrosion

In this study, we focused our attention to the role of residual stresses in accelerating corrosion initiation and progression in order to mimic the effect of accumulated residual plastic strain from dents or gouges. All corrosion experiments were carried out in a high pH electrolyte solution of 1 M NaHCO3 with pH 8.1-8.2 and applied potential in the range of -0.4 to -0.6 V vs. Ag/AgCl. We have started these experimental efforts in the last quarter. With further analysis of the data in Fig. 15, we have noticed strong and subtle changes in the current transients based on the residual plastic strain level. Focusing on the initial range of the current transients of Fig. 14, Fig. 15 shows a strong initial dependence on the pre-stain level.

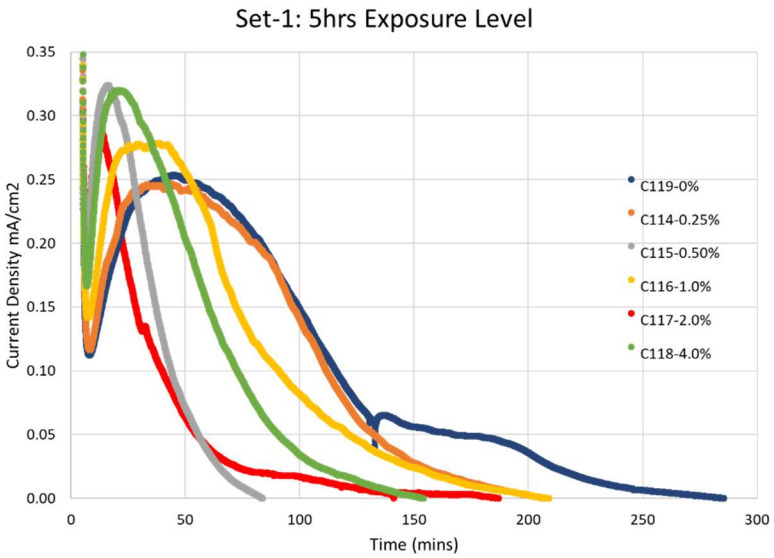

Figure 14: Results from accelerated corrosion testing on samples with accumulated plastic strains, simulating dents and gouges. The results show the strong dependence of the accumulated charges and, thereby, the corrosion rate on the accumulated plastic strain within the samples.

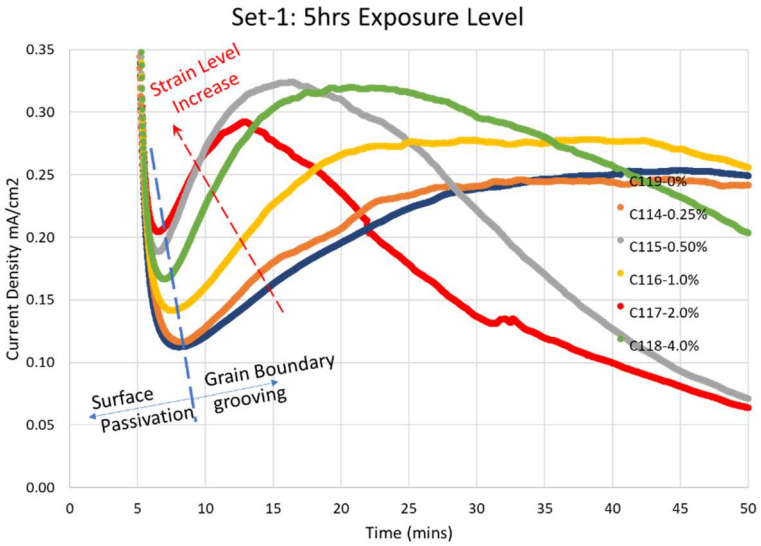

Figure 15: Magnified view of the initial current transit response of Fig. 14, highlighting the initial increase in the charge density responsible for GB grooving.

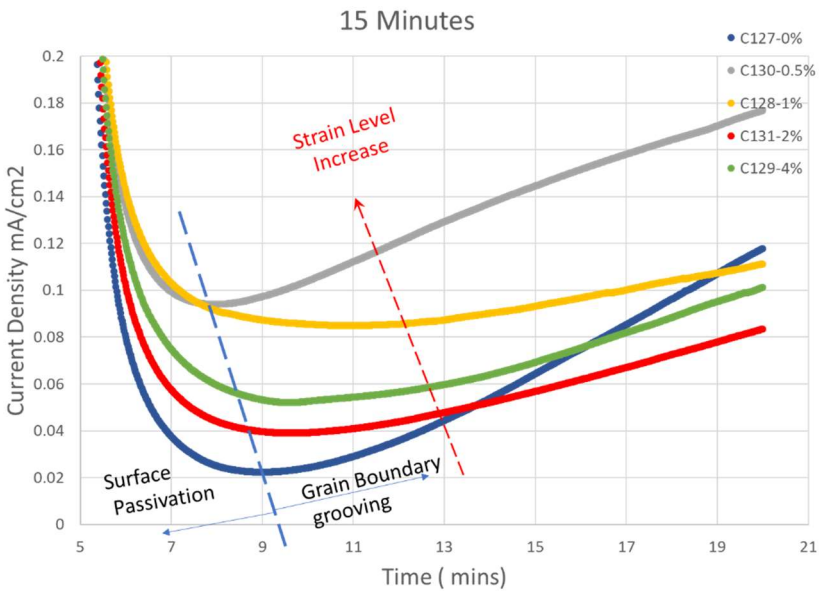

Figure 16: Short, accelerated corrosion experiments to reveal the surface morphological changes.

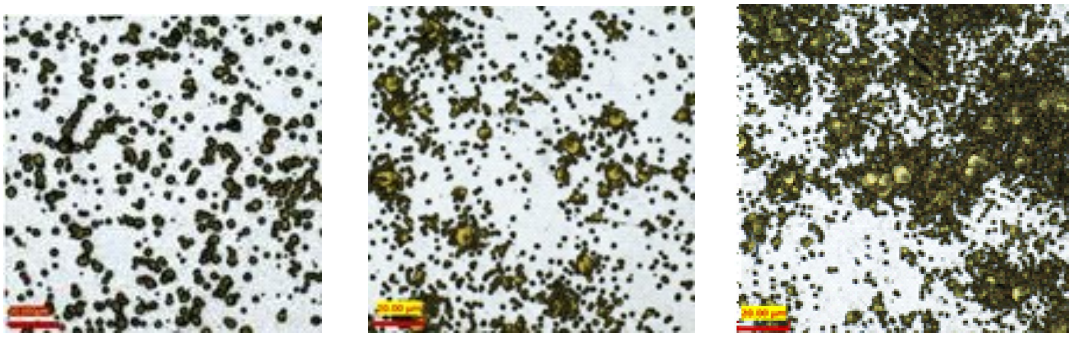

$\varepsilon_p = 0.0\%$ $\varepsilon_p = 1.0\%$ $\varepsilon_p = 4.0\%$

Figure 17: Optical images of the surface topological evolution as a function of the level or residual plastic strain in the samples. Dark spots are sites of active corrosion at the initial stage of the accelerated corrosion process, reported in Fig. 16.

Our hypothesis is that the increase in the current transient might have arisen from an increase in the active sites of corrosion due to the increase in dislocation density at the grain boundaries triple junctions. To understand such an effect, we have repeated two sets of short, accelerated corrosion experiments for 20 min of total exposure, and for different pre-strain levels of 0, 0.25, 0.5, 1.0, 2.0, and 4.0%. The current transients of one of these sets are shown in Fig. 16 and show the same initial strong dependence of the initial current transients with the level of pre-strains. The short corrosion exposure experiments enabled the retention of the original surface morphological features, especially the grain boundaries (GBs) triple junctions, before being overwhelmed with the progressive corrosion of the entire surface. The initial topological surface analysis shown in Fig. 17 indicates a strong correlation between the level of pre-strain and the density of the active corrosion sites.

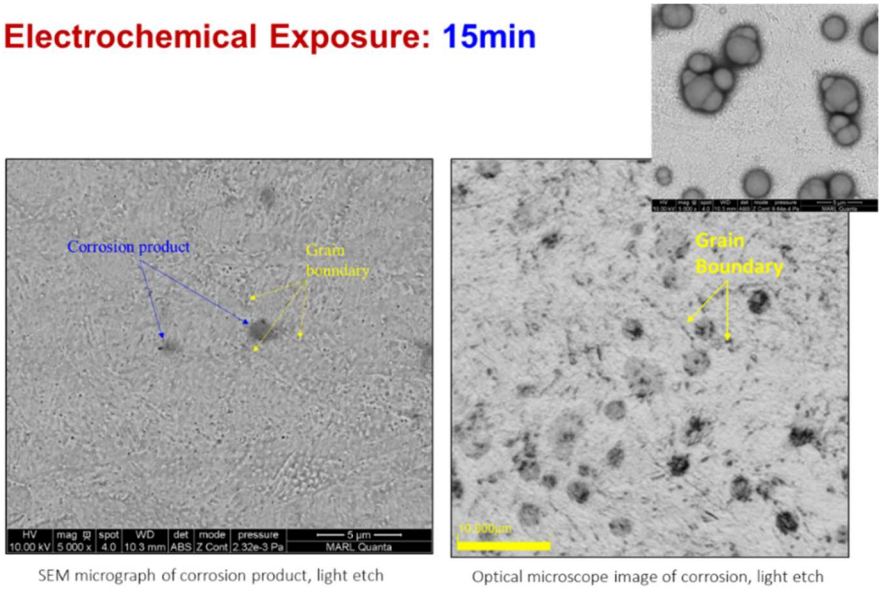

Figure 18: Optical and SEM analysis of the triple junction focused corrosion sites (lightly etched with acetic acid).

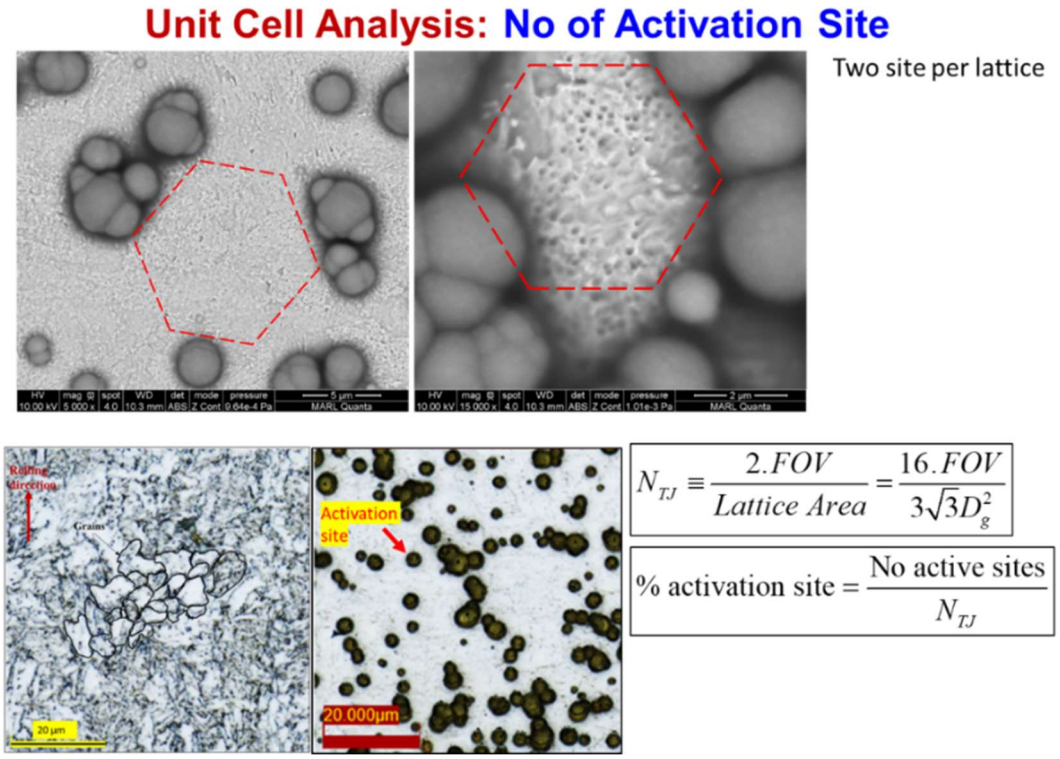

Figure 19: Unit cell analysis of the corrosion induced surface precipitates, and relating these sites to the density of the active corrosion site with respect to the grain size and observation window.

Figure 18 shows the evolution of these focused triple junction corrosion after 15min, visualized optically and after light etch with acetic acid. The active corrosion sites is clearly correlated with the grain boundaries triple junctions. We further analyzed the density of these corrosion sites per unit area to develop a metric for the percentage of activation sites in reference to the average grain size, as shown in Fig. 19. We assumed the surface grain structure to be modeled approximately by a hexagonal array. In such unit-cell analysis, each unit cell had two-lattice site, representing the density of triple junction per grain. This assumption has enabled us to assess the total number of available triple junctions or nucleation sites, $N_{TJ,}$ within the observed field of view (FOV). We proceeded to count the entire triple junction in each FOV at different levels of concentration for those shown in Figs. 17 and 21. We then plotted the density of the activation site as a function of the initial plastic strain, C (ε), as shown in Fig. 20. We were surprised to observe an Arrhenius dependence of C (ε) on the level of the pre-stain. This is a clear indication that the pre-strain level might have increased the density of the nucleation sites and accelerated the corrosion process.

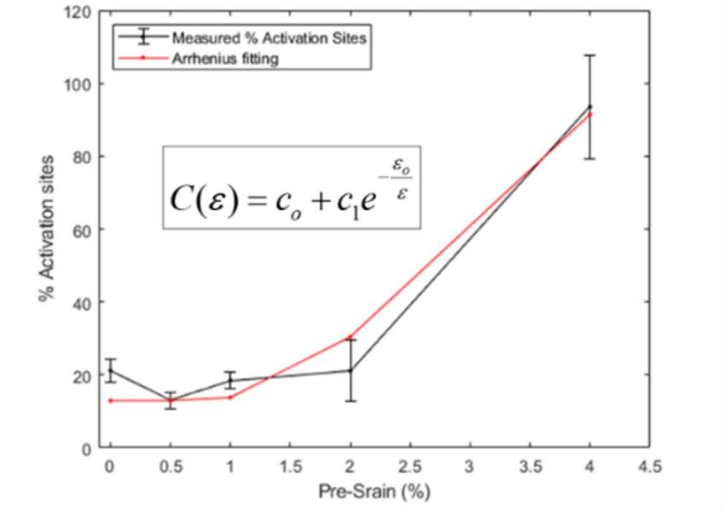

C(ε) is the percentage activation sites as a function of the prestrain level

C_o = reference site densities (0.13) ε_o = reference strain (0.06)

C_1= const. (3.51)

Figure 20: Arrhenius dependence of density of the triple junction corrosion site on the strain level.

Subsurface analysis of these two sets of samples was conducted to formulate a mechanistic understanding of the coupling between the level of accumulated plastic strains and the progression of corrosion. For the short time scale corrosion experiment, we saw initial precipitate, which we attempt to attribute to the activated grain boundary triple junctions. Figure 21 shows the focus ion beam (FIB) cut of a set of these precipitates as they appear on the surface and after the cut, revealing the underlying microstructure. Interestingly, we did not observe that these precipitates correspond to triple junctions, but rather, they are precipitated due to the active iron oxidation on the surface and start to precipitate on the surface at random sites. However, their densities are increasing with the level or the pre-strain. They are primarily indicative of surface diffusional

processes. The corresponding Energy Dispersive X-ray Spectroscopy (EDS) maps are shown in Fig. 22. No preferential sites for accumulation can be identified, especially for Si, which is indicative of surface diffusion processes.

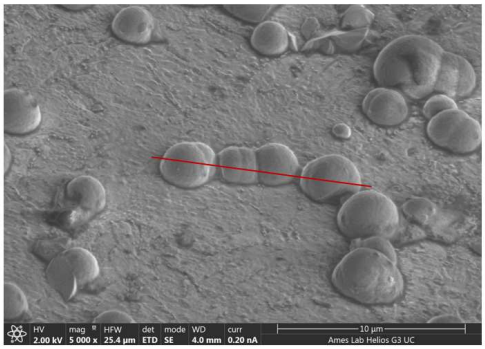

Sample surface as received. The red line shows the planned location for the FIB section.
NOTE: The sample is at 45° from horizontal.

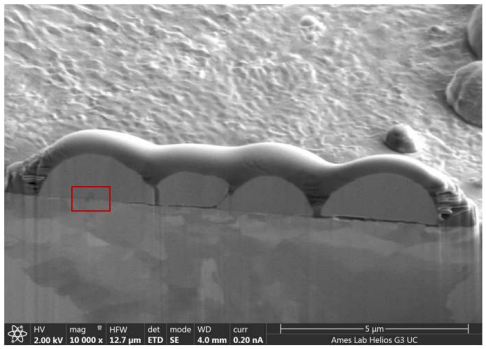

Sample surface after carbon deposition, FIB section, and initial polish. The rectangle highlights an area thought to be a locus of corrosion initiation.
NOTE: The sample is at 45° from horizontal.

Figure 21: FIB cut and subsurface imaging of the short exposure experiment with a reference state of 0% pre-strain. The surface precipitates do not correspond to GB triple junctions.

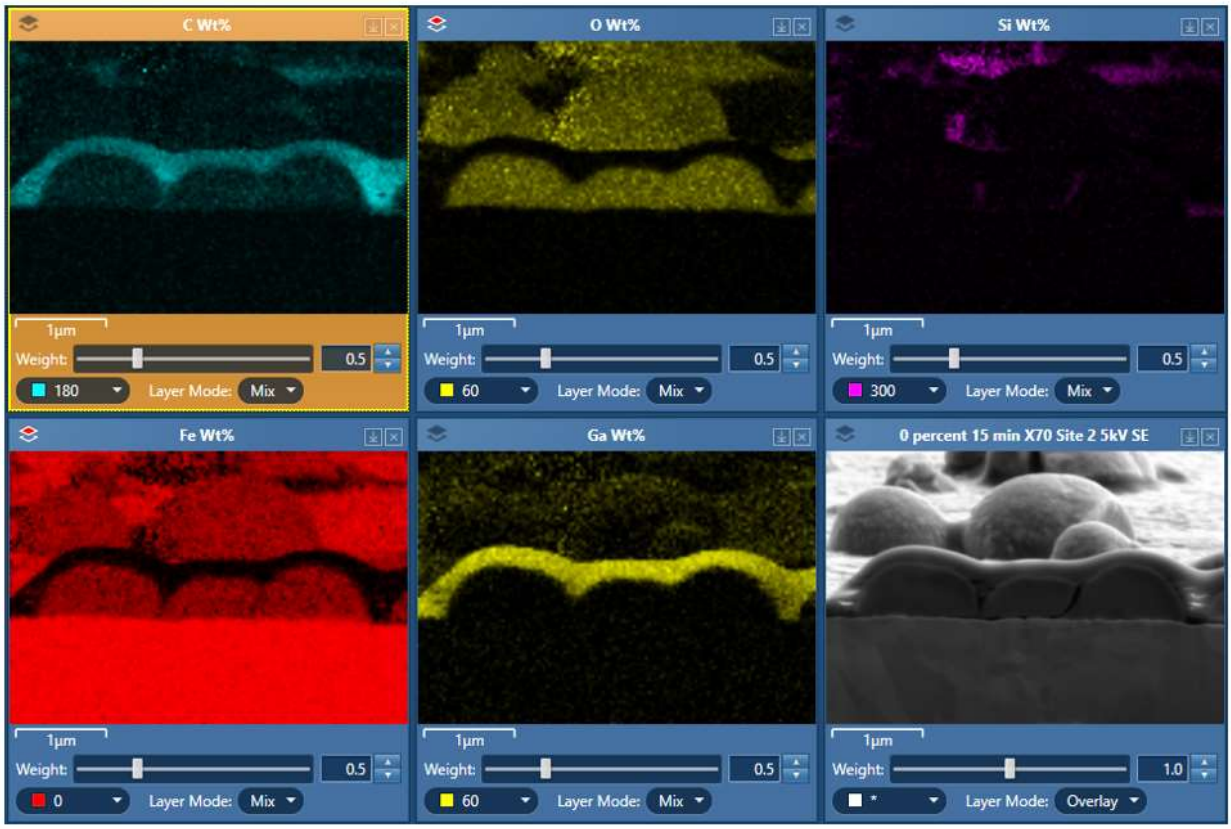

Figure 22: EDS maps for structure in Fig. 21. These are QuantMaps, where the spectrum at each pixel has been fully quantified. This removes some artifacts that may be caused by varying background intensities, peak overlaps, etc. The absolute concentration of Fe is clearly reduced in the corrosion product compared to the bulk Fe underneath, with the difference made up by C and O. Note that Ga is implanted by the Ga+ ion beam and mainly affects the carbon protective layer.

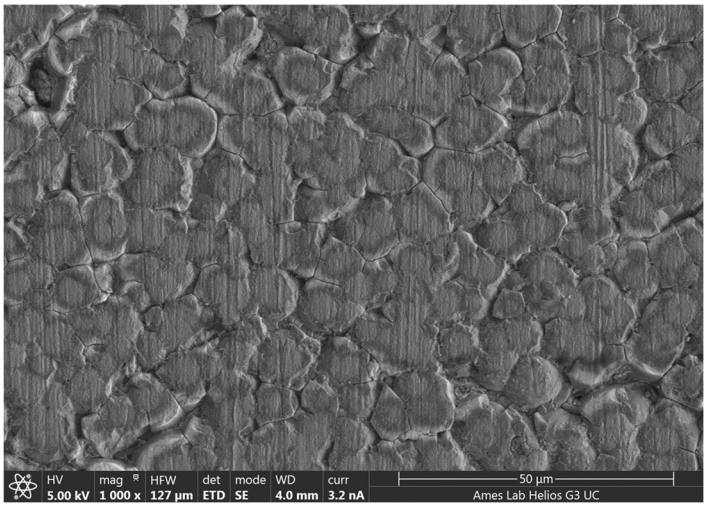

Figure 23: SEM image of the corrosion surface exposed to long electrochemical corrosion of 5 hrs. after removing the oxide layer with a tape lift-off. Corrosion rings are prominent around each Fe core. Intergranular pits and concentrations of other elements (likely Si) are also visible.

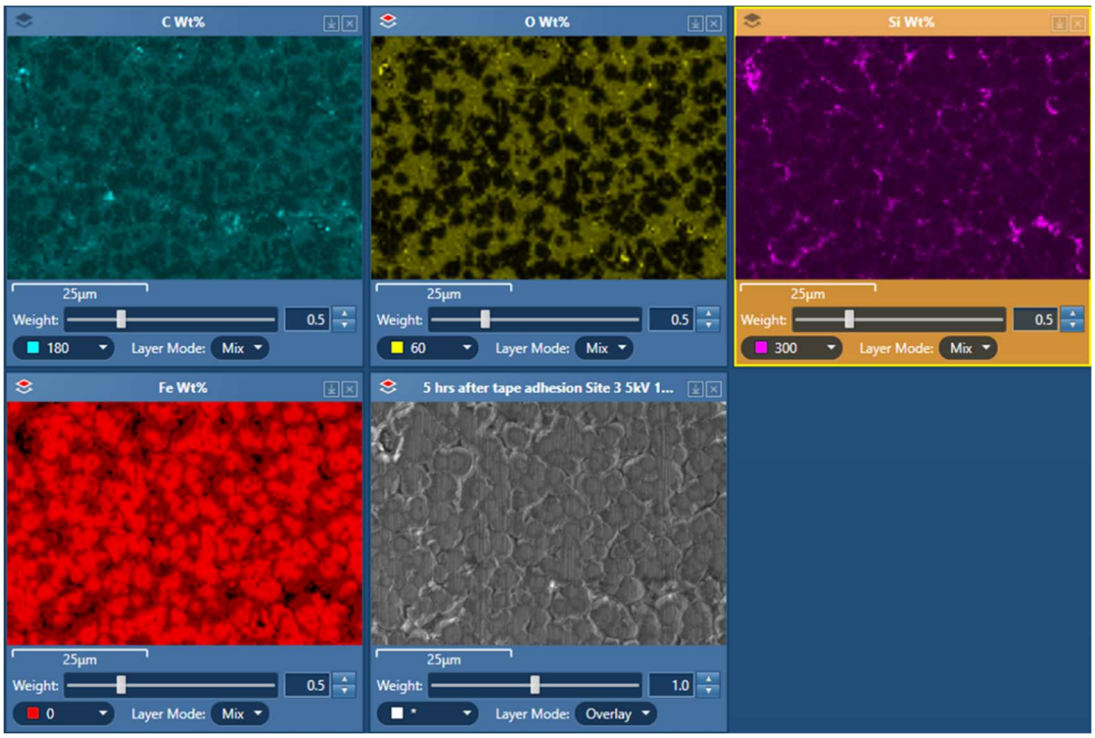

Figure 24: EDS maps for structure in Fig. 23 after long electrochemical corrosion of 5 hrs. These are QuantMaps, where the spectrum at each pixel has been fully quantified. Si is definitely concentrated in the grain boundaries. Fe grains have a core rich in Fe, surrounded by a ring of $FeCO_3$. Pores appear to be Fe-deficient, though this interpretation is complicated by topography.

For the 5-hours exposure sample, we used a lift-off tap to remove the product layer and examine the underlying morphology, as shown in Fig. 23. The triple junction and GB corrosion can be clearly identified and visibly shown. Almost all triple junction sites are active. Figure 24 shows the elemental analysis by EDS, showing the strong concentration of Si at the GB triple junction.

We speculate that we have two concurrent mechanisms: (1) a surface diffusion-driven phenomenon, wherein a solute species such as Si is diffused from the bulk to the surface of the grain and is reduced. (ii) A GB diffusion, where Si is being reduced, leaving lattice vacancies behind. However, the process of GB grooving is accentuated by the formation of a full corrosion-induced product film layer with the associated residual film stresses. The interplay between these two mechanisms is responsible for the observed GB grooving and the percolation of IGSCC.

C.1.3 EIS Analysis of Corrosion Product Layer

Measurement of impedance spectra was initiated at the times marked in Fig. 9(b). The EIS collection times correspond to the current rise (5 min), current maximum (10 min), the initial rapid current decay after the maximum (30, 45, and 60 min), and the period of slowly decreasing low current density after this decay (90 and 120 min). Phase and modulus Bode impedance plots are shown in Fig. 25. On the basis of Kramers-Kronig tests, the residual error remained below 4% over the frequency range of 0.1 to 10^6 Hz. Data below 0.1 Hz were subject to higher residual errors due to the non-stationary base currents (Fig. 9(b)); thus, analysis of the impedance response was confined to frequencies no lower than 0.1 Hz. This range includes the diffusion-controlled portion of the spectra influenced by the corrosion product layer.

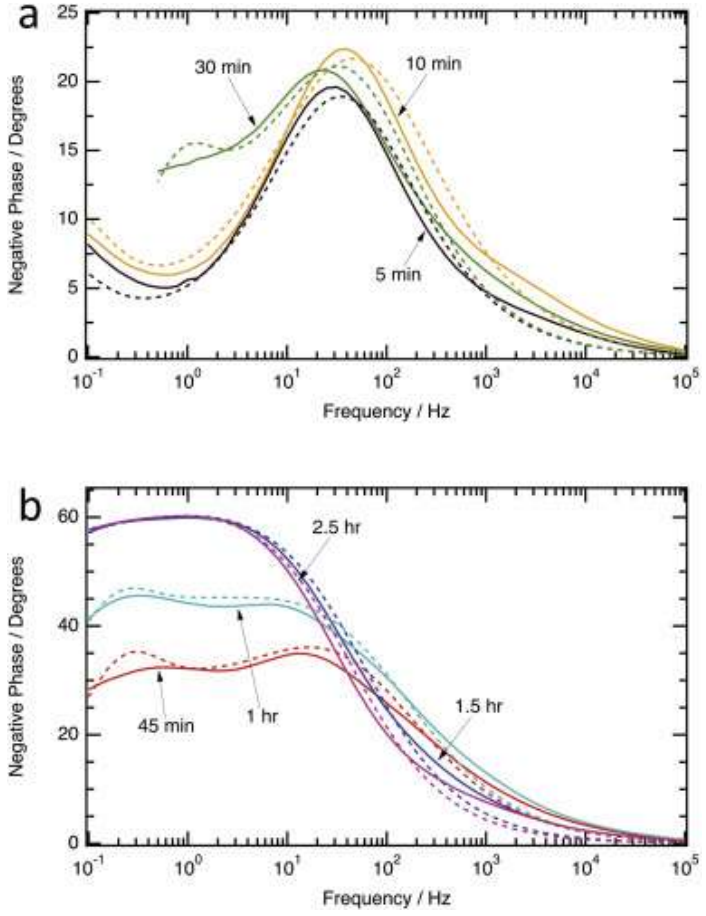

Figure 25: Phase angle vs. frequency at different exposure times 1 M $NaHCO_3$ at −0.521 V. Continuous curves represent experimental spectra, and dashed curves are model fits. (a) Small exposure times. (b) Large exposure times.

The impedance spectra exhibit several features with characteristic time constants, most evident as maxima in the phase plots (Fig. 25). Spectra for the short-time corrosion exposures of 5 min and 10 min are dominated by phase peaks at frequencies between 30 Hz and 40 Hz. The negative slopes at the lower limiting frequency of 0.1 Hz for the 5, and 10 min experiments suggest that a low-frequency phase peak may be present at around 0.01–0.1 Hz. The phase angle plots for exposures of 45 and 60 min include two maxima, at 0.2–0.5 Hz and at about 10 Hz. The shoulder in the phase plot of the 30 min experiment at about 0.5 Hz also suggests a relaxation in this frequency range. The phase curves for 90 min and 150 min experiments are similar to each other, each with a single maximum at around 1 Hz. Thus, the experimental spectra have at most two of the three relaxations in the model [35] with time constants τ_P, τ_{RC}, and τ_D.

The diffusion layer thickness δ and acceptor diffusivity D_A were calculated from the values of φ, τ_D, and the kinetic parameters. Table 1 lists separate values of δ and D_A corresponding to the choice of either bicarbonate or carbonate as acceptor anion. Also shown are estimates for each anion of the porosity of the precipitated layer based on the Bruggeman effective medium approximation, $D_A = \varepsilon^{1.5} D_A^o$, where D_A^o is the solution-phase diffusivity and ε is the porosity [36,37]. In the absence of a carbonate layer at small times, ε and δ should be of order 1 and 100 μm, respectively, the latter determined by the natural convection diffusion layer thickness [38]. At large corrosion times, δ should be of order 1 μm, the thickness of the corrosion product layer. Figure 26 shows that when carbonate ion is taken as the acceptor, ε, and δ are close to these expectations: ε decreases from 0.74 at 5 min to a consistent level of about 0.005 at 1–2.5 h, and δ decreases from 71 μm at 5 min to 1 μm at 30 min. Moreover, the increase of δ from 1 μm at 30 min to 5 μm at 2.5 h agrees well with experimentally observed growth of the carbonate layer from 2.5 to 4.3 μm between 2 and 4 h [39].

Table 1. Diffusion layer thickness, effective anion diffusivity, and corrosion product porosity were calculated from impedance parameters φ and τ_D. Results are shown for either bicarbonate or carbonate ion assumed to be the acceptor species.

Time (min)	Bicarbonate			Carbonate		
	δ (μm)	D_A (cm²/s)	Porosity	δ (μm)	D_A (cm²/s)	Porosity
5	0.42	1.8×10^{-10}	6.2×10^{-4}	71	5.2×10^{-6}	0.74
10	0.20	6.0×10^{-11}	3.0×10^{-4}	35	1.7×10^{-6}	0.35
30	7.6×10^{-3}	1.1×10^{-12}	2.1×10^{-5}	1.3	3.2×10^{-8}	0.025
45	9.5×10^{-3}	3.7×10^{-13}	1.0×10^{-5}	1.6	1.1×10^{-8}	0.012
60	5.9×10^{-3}	1.1×10^{-13}	4.5×10^{-6}	1.0	3.2×10^{-9}	5.4×10^{-3}
90	1.7×10^{-4}	6.9×10^{-14}	3.2×10^{-6}	2.8	2.0×10^{-9}	3.9×10^{-3}
150	3.2×10^{-4}	1.1×10^{-13}	4.5×10^{-6}	5.5	3.3×10^{-9}	5.4×10^{-3}

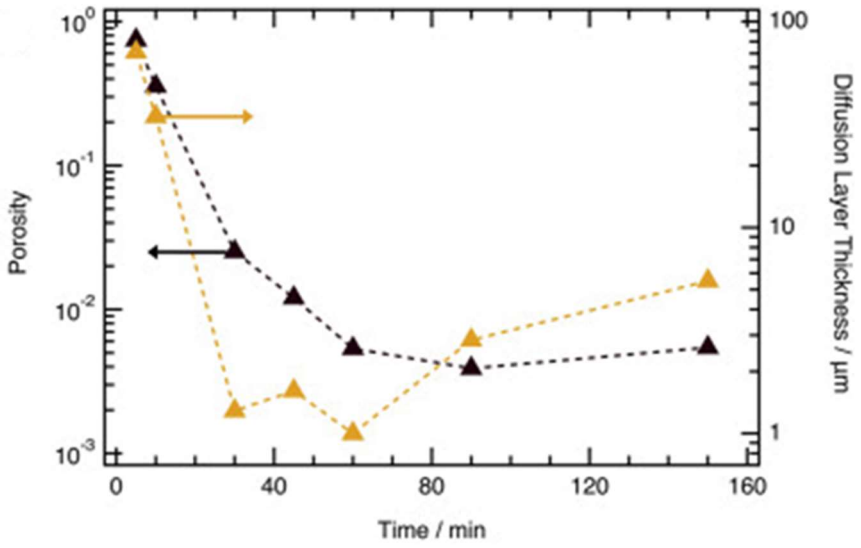

Figure 26: Dependence on corrosion time of estimated physical parameters from EIS. (a) Porosity φ and diffusion layer thickness δ.

It seems plausible that for both high-pH dissolution and CO_2 corrosion, EIS evolution may be controlled by the increasing diffusion resistance of the corrosion product layer. The present impedance analysis methods should then be highly useful for studies of corrosion product layer formation during CO_2 corrosion and in other electrochemical processes where precipitated surface layers serve as diffusion barriers.

(a) <u>Implications for crack initiations</u>

The impedance results demonstrate that the corrosion product layer grows at the metal interface by inward diffusion of CO_3^{-2} ions through the porous carbonate film. The product layer growth at the metal interface is due to the very low Fe^{+2} concentration of about 0.2 µM in equilibrium with $FeCO_3$ in 1 M $NaHCO_3$. We discuss next how carbonate layer growth at the metal interface is relevant to the high SCC susceptibility of pipeline steel at active dissolution potentials.

At active dissolution potentials, corrosion of X70 steel is centered at GB triple junctions, as shown in Fig. 23 for the potential of −0.521 V used in this work. Preferential corrosion at triple junctions produces grooves with triangular cross-sections filled with corrosion product wedges, as shown in Fig. 24. After prolonged corrosion exposures of X70 steel, intergranular cracks appeared at the base of the grooves, even in experiments with no external stress, as illustrated in Fig. 27 (a, b) for 5 h exposures in 1 M $NaHCO_3$ at −0.521 V. These cracks appeared after carbonate layer growth caused the current density to decay from a maximum at 0.4 mA/cm^2 to below 1 µA/cm^2. The formation of cracks without applied stress is attributed to tensile wedging stress due to the corrosion product occupying the GB groove [40], which will be further exacerbated in the presence of damage that induces tensile residual stresses. Figure 27 (c) illustrates how the growth of the $FeCO_3$ layer by inward CO_3^{-2} diffusion enhances wedging stress. Since the molar volume of $FeCO_3$ is 4.2 times larger than that of Fe, $FeCO_3$ formation at the metal-product layer interface is

accompanied by a large volume expansion. Close to the groove apex (e.g., point A), volume expansion of $FeCO_3$ out of the interface plane is blocked, and thus, out-of-plane compressive elastic stresses are generated in the steel. This, in turn, produces tensile stress at the GB ahead of the groove apex (point B) [41], creating the driving force needed to form the cracks in Fig. 27(a, b). Cracks also initiate at corrosion-generated GB grooves in SCC tests under external load [42]; in this situation, tensile stress at the GB is increased by the combination of both wedging stress and external stress concentrated by groove geometry itself. Grain boundary cracks would be expected to relieve compressive stress in the carbonate layer and hence may increase its porosity so as to assist the propagation of corrosion in the GB. Similarly, applied cyclic loads may also increase the porosity and/or increase the fragmentation of the carbonate layer, and thereby further exacerbating the GB cracking nucleation and propagation process.

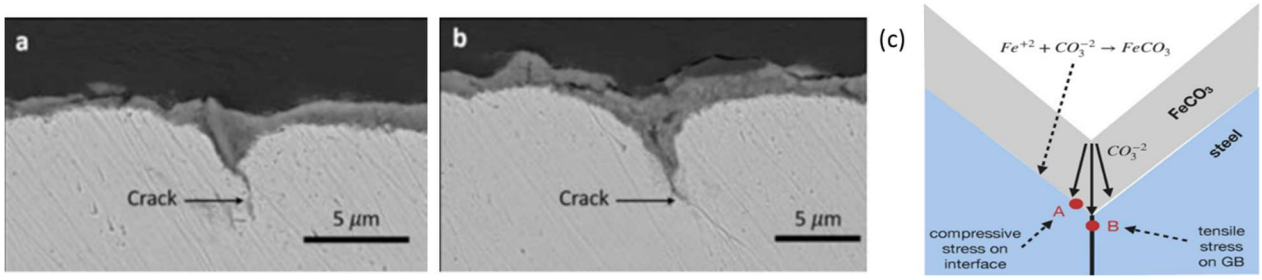

Figure 27: (a, b) SEM images of large-angle cross sections of X70 steel after 5 h corrosion at −0.521 V in 1 M $NaHCO_3$. (c) Illustration of the groove formed by corrosion at grain boundary triple junction. $FeCO_3$ corrosion product layer grows at the metal interface by inward diffusion of CO_3^{-2} ions. Close to the triple junction (point A), volume expansion of the corrosion product leading to compressive out-of-plane stress in the steel and a tensile stress concentration at the GB ahead of the wedge (point B).

Since the wedging stress mechanism depends on the presence of carbonate layers in GB grooves, it explains why the cracks in Fig. 27 (a, b) form after current density decays caused by the buildup of the carbonate layer diffusion resistance. Crack initiation at low current density may conflict with the view that intergranular cracks in pipeline steels grow directly by dissolution [43]. On the other hand, active dissolution is required to create the GB groove geometry necessary for wedging stress. This can help explain the high susceptibility to SCC at active dissolution potentials. The particularly high SCC susceptibility at potentials between the active peak current density and the passivation potential [43] may be due to the increased presence of less soluble Fe (III) compounds at such potentials, which would promote solid corrosion product formation. Indeed, we found a significantly reduced coverage of corrosion products at a potential of −0.575 V, close to the peak potential [39]. It should also be mentioned that tensile wedging stress in the GB should increase markedly with decreasing groove angle. *An analysis of time-dependent corrosion product-induced stress, incorporating the effect of groove shape change, can potentially predict the time of crack initiation.*

C.2 Simulation Results and Analysis of Dent Effect on Fatigue Life of Steel Pipelines

C.2.1 Parameter calibration for the elastoplastic material model

The original plan of this task was to use results from lab-scale experiments to construct and calibrate the fatigue damage model, including monotonic tensile and fatigue loading steps. However, our industrial collaborator proposed to employ the extensive full-scale testing data and try to understand the root cause of these interactive effects. Accordingly, the developed continuum damage model was validated in two steps, (i) against the experimental monotonic tensile tests of lab scale samples and/or indentation of a full scale pipes, in order to reproduce the base elastic-plastic strength and toughness response, and (ii) the fatigue data that were obtained from the literature [24, 33]. This data set provided a wider range of design space that far exceed what could be generated in a limited lab test, including: (i) Availability of fatigue data at different *R-ratios*, which was necessary to complete the validation process. (ii) Availability of full-scale testing data for different grades of steel (X52 and X70) with different dent depth and corrosion characteristics. Additionally, in order to confirm the accuracy and applicability of the computational elasto-plastic damage framework, we conducted further calibration and demonstrated the flexibility of the model in explaining the impact of pre-accumulated plastic strain on the anticipated fatigue life. This analysis was conducted using a well-documented dataset [32] pertaining to a different material system, specifically Titanium super-alloy, Ti-6Al-4V. For this data set, the initial plastic strain was uniformly applied on to the tensile gauge. The resulting deformation field was homogenous without any geometrically induced residual stresses. The verification for this Ti-based alloy is separately highlighted in section C.2.2(c) for the detailed

As noted above, two sets of material parameters should be calibrated. The first set is the parameters of the elastoplastic constitutive model, such as isotropic and kinematic hardening parameters. This will be done employing the monotonic tensile tests of the base metals. It could be also accomplished from the data set of a full-scale pipe indentation test. The second set is the fatigue damage model parameters with the addition of the combing the material damage induced by initial plastic strains (arising from dents and gouges) and those arising from the fatigue induced damage. A brief illustration of the parameter calibration process are introduced in the next subsections (a)-(c).

(a) <u>Hardening parameters calibration for the elastoplastic constitutive model</u>

To calibrate the elastoplastic model, we employed the published data set Bolton et al. [24], along with a series of numerical indentation simulations for X52 and X70 pipeline steels. In this calibrated model, only the kinematic hardening equation with two back stresses were used. Table 2 presents the material constants and the calibrated hardening parameters, C_k and γ_k.

Table 2: Material parameters of the elastoplastic constitutive model for X52 and X70

Parameter	E (GPa)	σ_y (MPa)	σ_u (MPa)	C_1(MPa)	C_2(MPa)	γ_1	γ_2
X52	200	400	567	13000	150	150	20
X70	200	450	620	20000	7000	500	200

A pipe model with a diameter of 609.6 mm, a wall thickness of 9 mm, and a total length of 3100 mm was created. The dimensions of the pipe mimic the actual pipe model that was used to perform the experimental testing reported in [24]. A schematic model of the pipe is shown in Fig. 28. For computational efficiency and with the advantage of pipe symmetry, only one-quarter of the pipe was created. In addition, to eliminate the effect of boundary conditions, the length of the pipe was chosen to be ten times the diameter of the pipe. The pipe was then discretized using eight-node linear hexahedral brick elements (C3D8) with a global element size of 15 mm. The mesh was further refined under the region of contact between the pipe and the indenter with an element size of 6 mm, as shown in Fig. 28b. An axisymmetric boundary conditions were applied along the axial and the transverse directions, while the displacement in the y-direction is restricted at the bottom of the pipe. Afterward, a contact was defined between the spherical rigid indenter and the outer surface of the pipe with a friction coefficient of 0.3. During the indentation, the indenter was pushed downward to a maximum displacement of 90 mm and then pushed upward to allow for the elastic recovery of the pipe. The force-displacement curves for X52 and X70 steels were extracted and plotted over the experimental responses, as presented in Fig. 29. As can be indicated, the pipe starts to deform linearly under the indentation loading as the force increases linearly with the displacement. As the indentation load increases, the deformation of the pipe becomes nonlinear, which reflects the buckling of the pipe under a higher indentation load. The transition from indentation to shell buckling can be seen as a knee in the force-displacement curves at ~8 mm indentation depths, as shown in Fig. 29. The simulation results for the force- indentation depth response, employing the calibrated elastoplastic constitutive model matches well with macroscopic response, obtained from the full-scale pipe indentation experiment. As such, the calibrated model can be confidently used to further calibrate the coupled fatigue damage model.

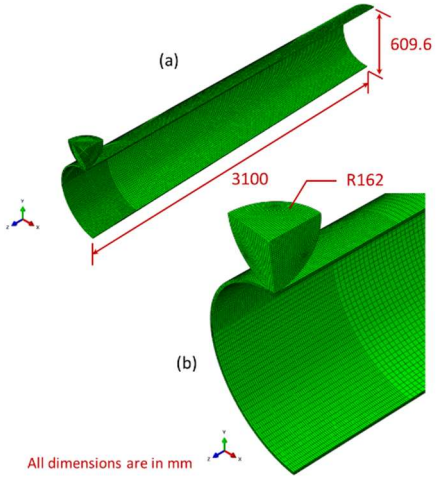

Figure 28: The geometric model of the pipe. (a) Full model; (b) Enlarged view of the dented region of interest.

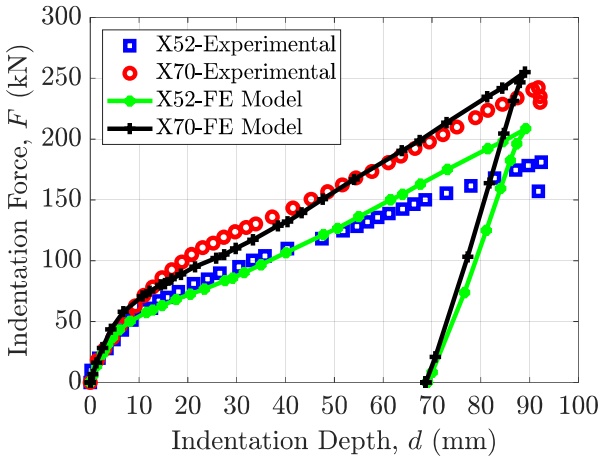

Figure 29: Force displacement responses during the indentation process for X52 and X70 steels. Experimental data is adopted from [24].

(b) <u>Parameters calibration for the elastic fatigue model</u>

The parameters for the elastic fatigue model are calibrated through a set of uniaxial tensile simulations for X52 and X70 steels. For the uniaxial fatigue loading scenario, the number of cycles to failure, N_f, can be obtained by integrating Eq. (30) from $D^e = 0$ to $D^e = 1$. The corresponding N_f will be given by,

$$N_f = \frac{1}{(1+\beta)aM_o^{-\beta}} \frac{\langle \sigma_u - \sigma_{max} \rangle}{\langle \sigma_a - \sigma_{lo}\left(1 - b_1(\overline{\sigma}/\sigma_u)\right) \rangle} \left(\frac{\sigma_a}{1 - b_2\overline{\sigma}}\right)^{\beta}. \tag{41}$$

The ultimate tensile stress, σ_u, is obtained from the monotonic stress-strain response of the tested material. The fatigue endurance limit, σ_{lo}, is obtained from the experimental fatigue data at fully reversed loading (i.e. R = -1). Subsequently, the unknowns parameters (β and $aM_o^{-\beta}$) can be directly computed. Furthermore, parameters b_1 and b_2 are estimated using Eq. (41) through least square fitting of the fatigue experimental results at two different and non-zero means stresses (i.e. R > -1). Finally, using finite element simulation of a straight sample, the value of a is identified numerically as the value that provides the same fatigue life for a straight sample as computed from Eq. (41). In the current work, the experimental fatigue S-N data of X52 and X70 are adopted from [26, 27] and [28, 29], respectively and are used to calibrate the parameters for the elastic damage evolution model for the two different grades of steels. A standard tensile fatigue specimen was created based on the standard provided by ASTM E466 [18]. The sample has a total length of 216 mm, a gauge length of 30 mm, a gauge height of 15 mm, and a thickness of 6 mm. A schematic model of the specimen is shown in Fig. 30. The fatigue specimens were discretized using C3D8 eight-node linear brick element, with a refined mesh in the gauge region. A mesh sensitivity analysis was conducted, and the damage evolution was found to be insensitive to the element size of the mesh. An encaster boundary condition was applied to the left grip, while only the displacement in the *x*-direction was allowed for the right grip.

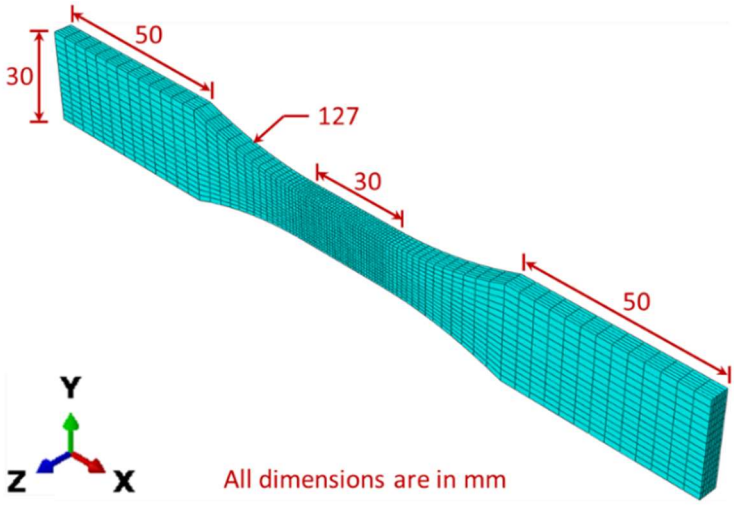

Figure 30: The geometric model of the standard tensile fatigue specimen. The specimen was created according to the ASTM E466 standard [18].

A user material subroutine (UMAT) was developed to implement the fatigue damage model into the finite element framework through Abaqus software. In the UMAT, the stress and strain are computed at each integration point and then used to solve the damage evolution equations. Afterward, the accumulated damage over time is used to degrade the elastic modulus of the material,

$$E^{i+1} = E^{i}\left(1 - D^{i+1}\right). \tag{42}$$

Damage evolution equations (30) and (39) are solved numerically using a backward difference scheme. An initial damage value of 10^{-6} was utilized to avoid any singularities in the first loading cycle. Once the damage variable reaches the saturation limit of *1* at any integration point, a macroscopic fatigue crack is deemed to have occurred at such material point.

Figures 31 and 32 present the comparison of the S-N curves of uniaxial fatigue simulations at two different loading ratios for X52 and X70, respectively, as predicted by the damage evolution model presented in Eq. (30) and the experimental results provided in [26,27] for X52 and in [28,29] for X70. The calibrated fatigue responses for the two steel grades exhibit good fit with the experimental results.

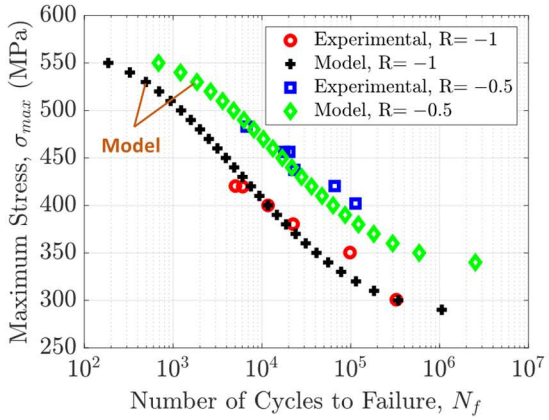

Figure 31: S-N curves for the X52 at two different loading ratios ($R = -1$ and $R = -0.5$). The black crosses and green diamonds stand for the data obtained from the model. The red circles and blue boxes refer to the experimental data at the same loading ratios adapted from ref. [26, 27]

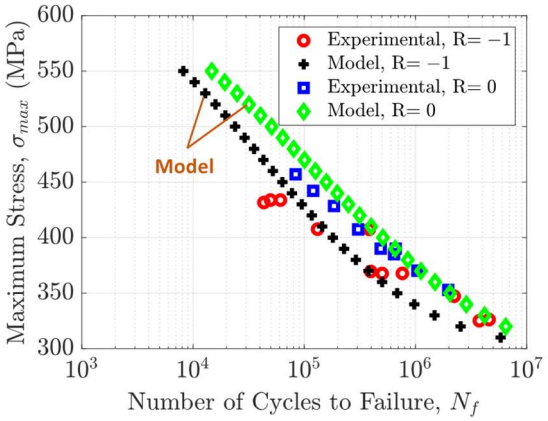

Figure 32: S-N curves for the X70 at two different loading ratios ($R = -1$ and $R = 0$). The black crosses and green diamonds stand for the data obtained from the model. The red circles and blue boxes refer to the experimental data at the same loading ratios adapted from ref. [28, 29]

For computational efficiency, a cycle jumping technique was adopted, where the stress and strain fields are assumed to remain constant over a block of cycles such that the accumulation of damage is calculated,

$$D^{i+1} = D^{i} + \left(\frac{dD^{e}}{dN} + \frac{dD^{p}}{dN}\right)\Delta N. \tag{43}$$

Here, ΔN is the cycle block, D^{i} is the total damage from the previous block of cycles, and D^{i+1} is the total damage at the current ΔN.

Cycle jumping with a variable ΔN were employed in previous fatigue studies. However, the damage model yields approximately the same analytical results up to $\Delta N/N_f = 0.04$ [16]. Therefore, in current work, a relatively small and fixed cycle block $(\Delta N/N_f \approx 0.015)$ was used to maintain numerical efficiency. Moreover, the damage equation requires a full solution for stress components over the fatigue cycle (loading-unloading) to compute the maximum shear stress amplitude, τ_a, and mean hydrostatic stress, $\sigma^D_{H,mean}$, within the cycle. Nevertheless, solving the full cycle is computationally demanding, even with the utilization of the cycle jumping method. As such, a simplified strategy such that the minimum and maximum stress tensors at an integration point are coupled through the loading *R-ratio*, as follows,

$$\tau_a = \frac{1-R}{2}\sigma^D_{eq,max}\,, \tag{44}$$

$$\sigma^D_{H,mean} = \frac{1+R}{2}\sigma^D_{H,max}\,. \tag{45}$$

The adopted simplified relation is valid for linear elastic and proportional loading [9]. In this way, the stress and strain fields and the subsequent damage evolution are only computed at one point in the cycle (maximum stress), resulting in a great reduction in the computational time.

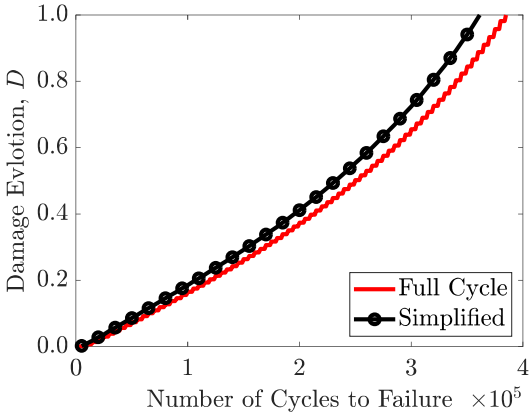

Figure 33: The comparison of the evolution of damage evolution versus the number of cycles for the notched fatigue specimen with a maximum stress $\sigma_{max} = 800$ MPa and loading ration, $R = -0.5$, as predicted by solving the full loading-unloading stress cycle and by the simplified algorithm. The presented data is obtained at the central nodal point in the notch of the specimen.

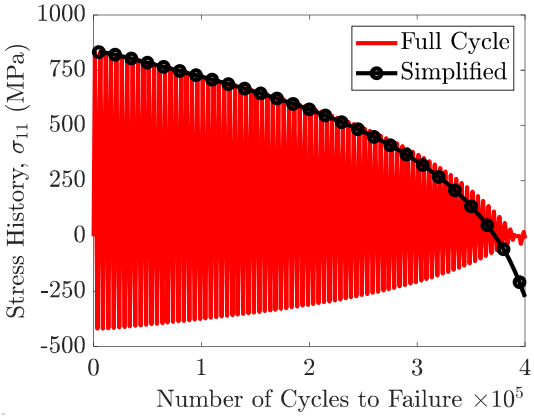

Figure 34: The comparison of the stress history in the loading direction versus the number of cycles for the notched fatigue specimen with a maximum stress $\sigma_{max} = 800$ MPa and loading ratio, $R = -0.5$, as predicted by solving the full loading-unloading stress cycle and by the simplified algorithm. The presented data is obtained at the central nodal point in the notch of the specimen.

Figures 33 and 34 present the damage evolution and stress history, respectively, for a notched specimen subjected to 800 MPa maximum stress and $R = -0.5$. The damage linearly evolves up to 20% of the total damage. However, it exhibits higher nonlinear accumulation as the number of cycles approach N_f.

(c) Parameters calibration for the plastic-damage fatigue model

The Coffin–Manson law for low cyclic fatigue was used to calibrate the parameters in the plastic damage model for strain based fatigue life.

$$\frac{\Delta\epsilon_p}{2} = \epsilon_f(2N_f)^c \tag{46}$$

where $\Delta\epsilon_p/2$ is the plastic strain amplitude, ϵ_f is the fatigue ductility coefficient (the failure strain for a single reversal), $2N_f$ is the number of reversals to failure (N_f cycles), and c is the fatigue ductility exponent.

The number of cycles to failure in Eq. (46) can be obtained by integrating Eq. (39) from $D^p = 0$ to $D^p = 1$. The corresponding N_f will be given by,

$$N_f = \frac{1}{2(2m+1)\Delta\overline{\epsilon}_p}\left(\frac{2ES}{(\sigma_{max})^2}\right)^m. \tag{47}$$

Furthermore, the relation between stress and strain in cyclic plastic deformation is described using the Ramberg-Osgood relation,

$$\sigma_{max} = K'\left(\frac{\Delta\epsilon_p}{2}\right)^{n'} \tag{48}$$

where K' and n' are material parameters representing the hardening coefficient and the hardening exponent, respectively. Using such relation, N_f can be expressed in terms of $\Delta\epsilon_p$,

$$N_f = \frac{1}{2(2m+1)}\left(\frac{2^{1+2n'}ES}{K'^2}\right)^m \left(\Delta\epsilon_p\right)^{-(1+2mn')}. \tag{49}$$

The values for K', n', ϵ_f, and c are adopted from ref. [30] for X52 and from ref. [30, 31] for X70 and subsequently, Eq. (49) is solved at two different points in the low cyclic fatigue regime to calibrate the values of S and m. Finally, the calibrated parameters for the elastic and plastic fatigue damage models for the two steel grades are presented in Table 3.

Table 3: Material parameters of the fatigue-coupled damage model for the X52 and X70

	Elastic fatigue damage parameters					Plastic fatigue damage parameters	
Parameter	a	b_1	b_2(MPa^{-1})	β	M_o(MPa)	S (MPa)	m
X52	0.75	1.32	0.000029	3.22	9341	0.445	3.32
X70	0.72	1.28	0.0014	3.25	18357	0.660	6.56

C.2.2 Dent effect on the fatigue life

After validating the coupled damage-elastoplastic model, the effect of dents on the remaining fatigue life of steel pipelines was investigated through a series of fatigue simulations at different dent depths, and the obtained results were then compared with experimental data. The effect of dent conditions (restraint or unrestraint) on the plastic strain levels and the subsequent plastic damage were investigated. In these simulations, the geometric model of the pipe, presented in Fig. 28, was first indented to a desired indentation depth, followed by indenter release to allow for the elastic recovery. Afterward, the indenter was either completely removed or kept in place to simulate the unrestraint or the restraint conditions, respectively. Two cycles of internal pressure were subsequently applied to facilitate the pressure-induced rebounding of the dent. The applied pressure was set to induce hoop stresses within the pipe-walls as ratio of the yield strength of the pipe material. For unrestraint condition of the dent, the final dent depth was calculated after the rebounding pressurization step, where different pressures result in different dent depths. Lastly, cyclic internal pressure, corresponding to hoop stress of 10% - 80% of the yield strength is applied to simulate the fatigue loading on the dented pipe.

(a) <u>Dent profile under pressure-driven rebounding</u>

Figure 35 shows the surface displacement profile along the pipe axis (z-axis of Fig. 28) of during the dent formation process. After the indentation process and the removal of the indenter, elastic recovery reduced the indentation depth by about 20%. When a pressurization step was followed after the indentation, the final dent depth was further modulated by the pressure-driven rebounding stages. For example, the final dent depth was decreased from 98 mm after the elastic recovery to 48 mm and 20 mm when pressure levels corresponding to hoop stresses of 40% and 75% of the yield strength are applied, respectively, as shown in Fig. 35. In addition, as the pressure level increases, a plastic hinge appears in the dent shoulder. This plastic hinge is shown to accommodate higher level of plastic strain, which will affect the initial plastic damage and the subsequent fatigue life, as will be shown later.

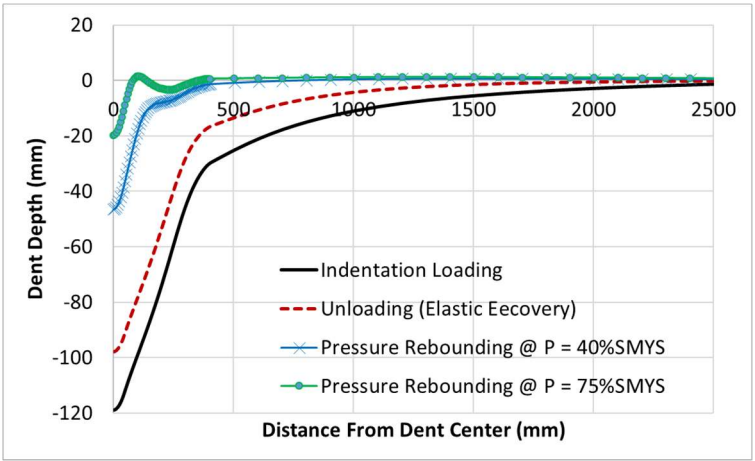

Figure 35: The axial profile of the dent at three different stages of the dent formation process. The vertical axis is the displacement in the vertical direction (y-axis in Fig. 28), which represents the depth of the dent, and the horizontal axis is the measure of the horizontal distance from the center of the dent along the axial direction of the pipe (z-axis in Fig. 28).

For the restraint dent condition, the final dent depth is the depth at the elastic recovery as the indenter restricts the deformation during the pressure rebound. As such, the initial plastic damage in the restraint case will be lower than in the unrestraint case, which will ultimately have a significant implication on the fatigue performance, as will be shown later.

(b) Strain response of dented pipes

During the indentation stage, the strain response of the model was compared with the experimentally measured strain during the indentation. Fig. 36 and Fig. 37 present the strain components in the hoop (x-axis) and the axial (z-axis) directions, respectively. Sanjay et al. [25] measured the hoop and axial strain during dent formation using strain gauges placed 100 mm away from the center of the dent on the outer surface of the pipe. The recorded strain values ranged from -4% in the hoop direction to +2% in the axial direction. At the same indentation depth and the same location of the strain gauge (100 mm from the dent center), the hoop and the axial strains obtained from the model were approximately -4.9% and +2.3%, respectively. It is worth noting that the maximum hoop strains are at the center of the dent, as shown in Fig. 36, and the maximum axial strain is located on the inner surface of the pipe at the point of contact between the indenter and the pipe, as shown in Fig. 37.

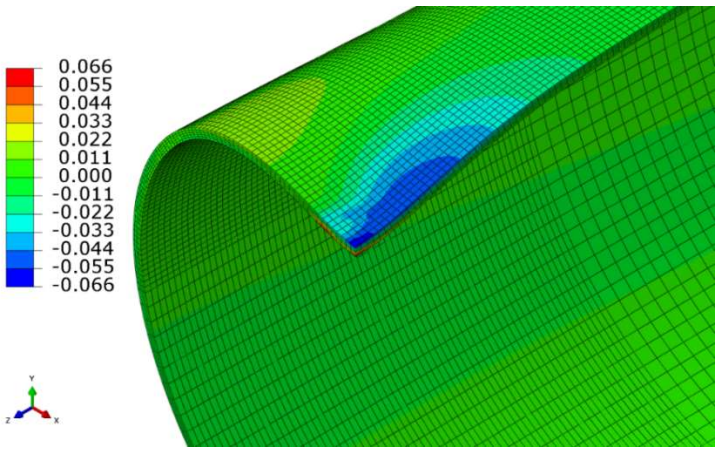

Figure 36: Hoop strain contours (ϵ_{xx}) during the indentation stage at a depth of 90 mm. The simulation in this plot is for X70 steel.

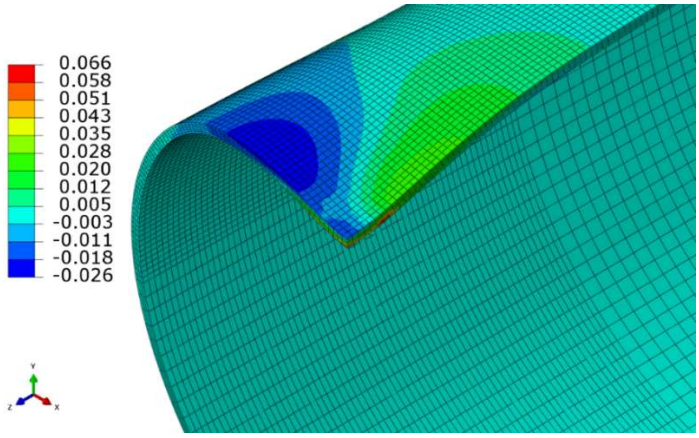

Figure 37: Axial strain contours (ϵ_{zz}) during the indentation stage at a depth of 90 mm. The simulation in this plot is for X70 steel.

After dent formation (indentation and pressure rebounding), the equivalent plastic strain was computed and then used to calculate the amount of plastic damage using Eq. (39), which will later be used as the initial damage for the fatigue loading part. This initial damage value represents the amount of fatigue life that will be lost due to the presence of external mechanical damage in the pipe, according to Eq. (40).

(c) Verification of the initial plastic damage role on the fatigue life for different material system

To illustrate the concept of the initial plastic damage effect on the fatigue life, a well documented experimental data set [32] is used for different material system (Ti-6Al-4V), where the examined cross-section has undergone homogenous state of initial plastic deformation, then subjected to oscillatory tensile loading. For comparison, we conducted a series of numerical simulations to estimate the total damage, D, and the subsequent fatigue life, N_f, at different levels of initial plastic strain. In these simulations, the tensile fatigue specimen was first loaded monotonically to a desired plastic strain value ($\Delta\bar{\varepsilon}_p = 0-3\%$). Then, from the accumulated plastic strain and stress state at this point, the initial plastic damage is computed using Eq. (39) and added to the total damage according to Eq. (25). Thereafter, the specimen was unloaded to remove elastic strains. Subsequently, the high cyclic fatigue loads were applied at $\sigma_{max} = 0.6\sigma_y$ ($\sigma_y = 804$ MPa) and $R = 0$, and the elastic fatigue damage was calculated using Eq. (30). Figure 38 presents the damage progression versus the fatigue life at different initial plastic strain values. As the figure shows, when the material has no initial plastic strain, the initial plastic damage is zero, and the material fails ($D = 1$) at ~4.5 million cycles. When the initial plastic strain increased to 1% and then to 3%, the initial plastic damage increased to 3.3% and 21%, respectively, and subsequently, the life was reduced to approximately 0.8 and 0.25 million cycles, respectively. In Fig. 39, the total life of the component is plotted against the initial plastic strain ranging from 0.2% to 5%. The total life was reduced by approximately 94% when the initial plastic strain increased from 0.2% to 5%.

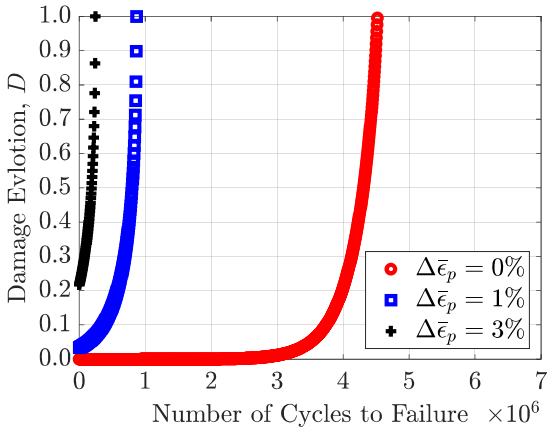

Figure 38: Damage evolution with respect to fatigue life at different initial plastic strain values. The results in this figure are obtained at $\sigma_{max} = 0.6\ \sigma_y$ and loading ratio, R = 0.

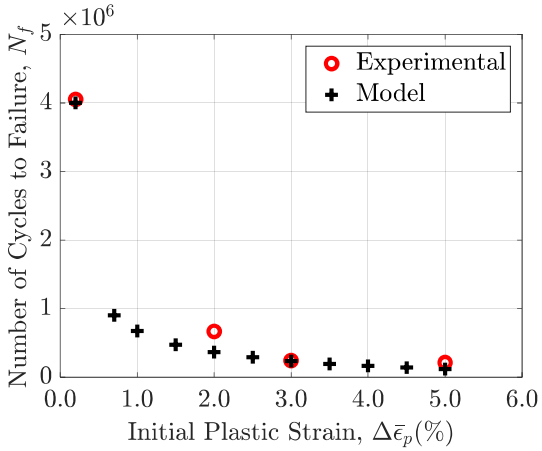

Figure 39: Model verification for the fatigue life prediction on a different material system (Ti-6Al-4V). Tensile high cyclic fatigue loads were applied at $\sigma_{max} = 0.6\ \sigma_y$ ($\sigma_y = 804$ MPa) and $R = 0$, [32].

(d) <u>Plastic damage progression during dent formation</u>

Figures 40 and 41 provide contour plots for the distributions of the Von Mises stress, the equivalent plastic strain, and the plastic damage index after indentation and pressure-driven rebounding stages for unrestraint and restraint conditions for the dented section, respectively. Figure 40a shows the accumulation of significant residual stress level around the shoulder of the dented region after the removal of the indenter. These elevated stresses were further intensified to higher levels after the dented was rebounded. The residual stress was increased from approximately 580 MPa in the dent shoulder along the circumferential direction to approximately 740 MPa, as shown in Fig. 40a and Fig.40b, respectively.

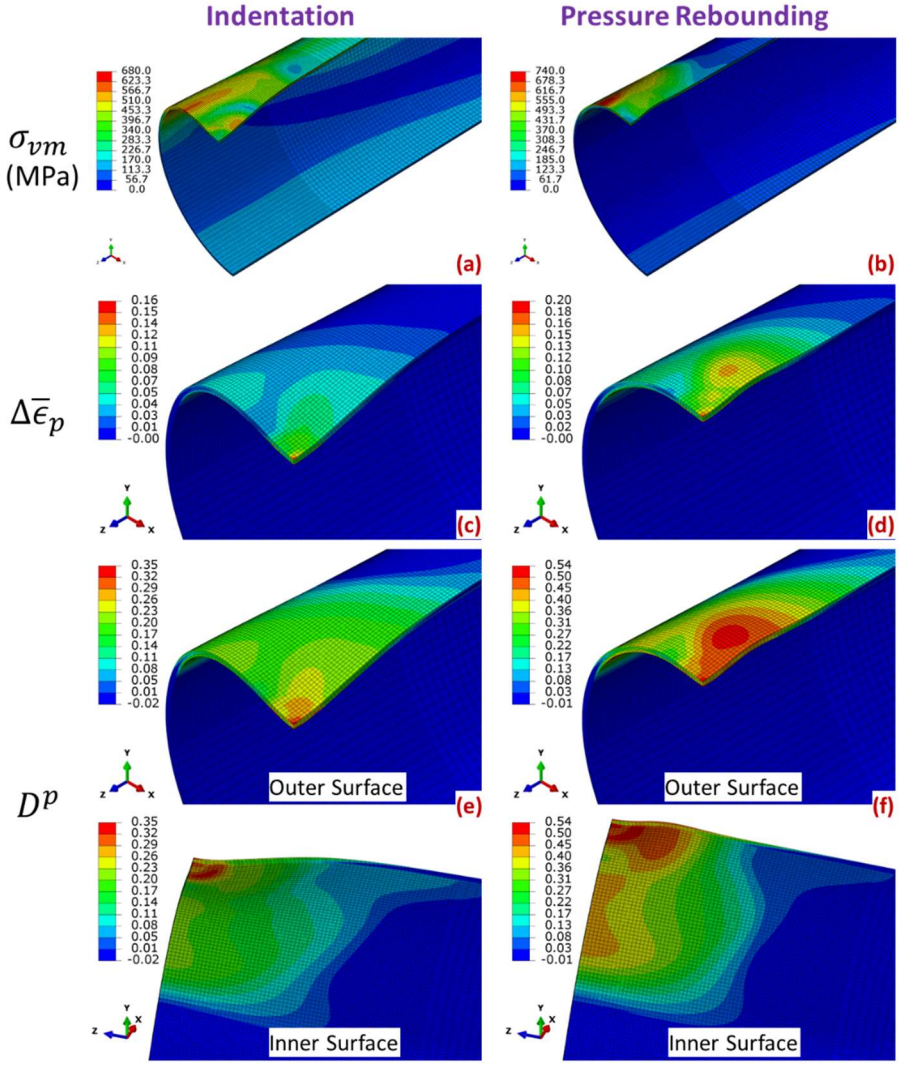

Figure 40: Distributions of the von-Mises stress, the equivalent plastic strain, and the plastic damage index for **an unrestraint** dent after indentation and pressure-driven rebounding. All simulations in this figure are for X70 steel pipe, which was indented to a maximum depth of 122 mm before the indenter was removed and the dent was elastically recovered. Afterward, the dent was rebounded by applying two cycles of internal pressure to a maximum hoop stress of 97% yield strength, before the internal pressure was removed.

The dent-induced residual stresses will severely affect the fatigue strength of the pipe. These residual stresses act as risers for the mean stress of the applied cyclic loading (i.e. increasing the *R-ratio*), which will ultimately result in a shorter fatigue life. Moreover, by inspecting the distribution of the equivalent plastic strain and the subsequent evolution of the plastic damage, some interesting findings were observed. *First*, the equivalent plastic strain evolves in the dent region during the indentation process and reaches approximately 6% around the center of the dent, as shown in Fig. 40c. *Second*, upon dent rebounding under the applied internal pressure, a plastic hinge appeared in the shoulder of the dent with a significant accumulation of equivalent plastic strain, reaching 15%, as shown in Fig. 40d. However, the average plastic strain within the dent region remains around 6-8%.

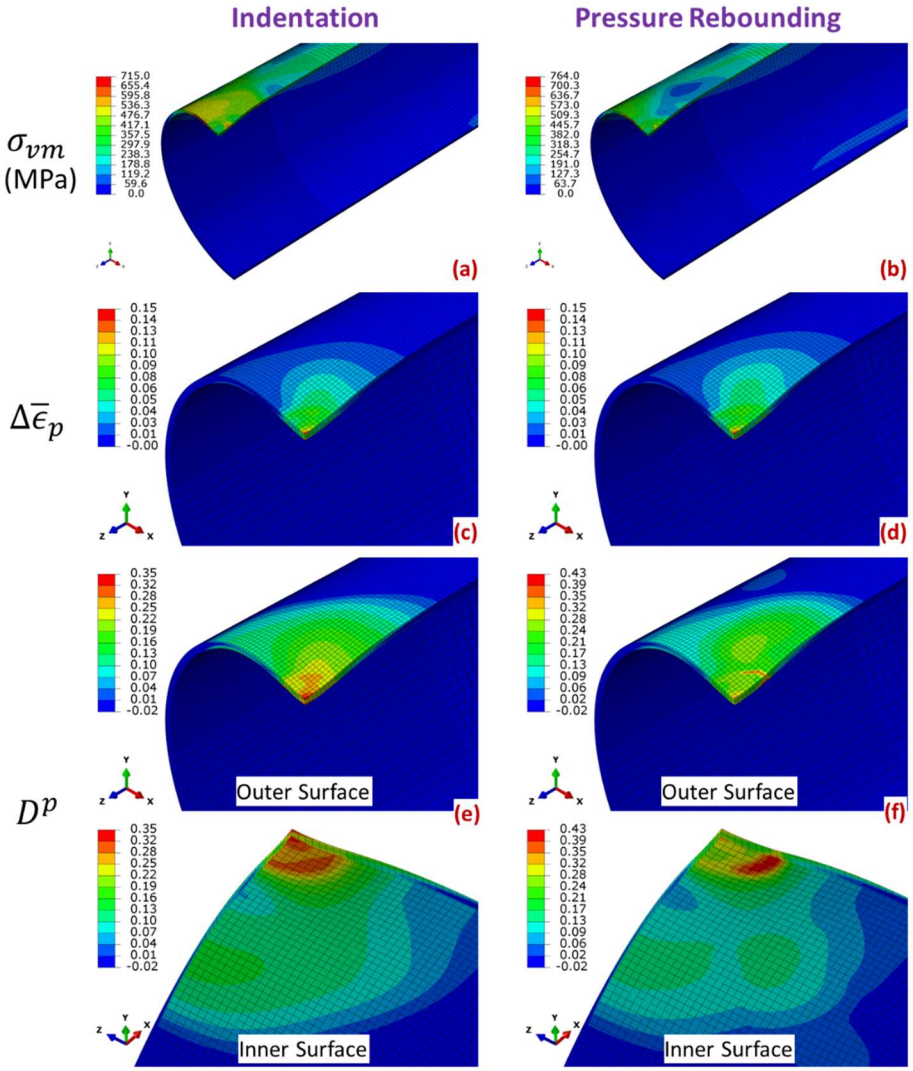

Figure 41: Distributions of the von-Mises stress, the equivalent plastic strain, and the plastic damage index for **a restraint** dent after indentation and pressure-driven rebounding. All simulations in this figure are for X70 steel pipe, which was indented to a maximum depth of 60 mm before the indented was slightly pushed upward to allow for elastic recovery. Afterward, the dent was rebounded by applying two cycles of internal pressure to a maximum hoop stress of 80% yield strength, before the internal pressure was removed. The indenter is eliminated for clarity.

Third, the plastic damage due to indentation evolves to approximately 35% around the center of the dent in the outer surface of the pipe, as shown in Fig. 40e. More importantly, there were significant increase of the accumulated plastic strain within the dent shoulder after the pressure rebounding process, as shown in Fig. 40d. As such, the plastic damage due rebounding will have a significant influence on the remaining fatigue life of the pipe and would drive fatigue cracks.

For the restraint dent condition, the distributions of the equivalent plastic strain and the subsequent plastic damage are quite different. As shown in Fig. 41a, b, the residual stress after indentation was approximately 710 MPa along the circumferential direction and jumped to ~760 MPa after pressure rebounding. Furthermore, the evolution of the plastic damage after indentation was shown to be comparable to the plastic strain level in the unrestraint dent, ~8% around the center of the dent, as shown in Fig. 40c and Fig. 41c, respectively. The plastic strain level remained constant after pressure rebounding, as shown in Fig. 41d. The evolution of the plastic damage followed the same behavior, where it reached approximately 20% around the center of the dent during the indentation and less than 10% after pressure rebounding, as shown in Fig. 41e, f, respectively. This implies that the total plastic damage in the restraint dent will be dominantly dictated by the damage caused by indentation. This is distinct from the unrestraint case, where the plastic damage from indentation and rebounding stages contribute to the total plastic damage.

Upon applying the fatigue loading, the total damage starts to increase. Figure 42 shows the fatigue damage progression as false color maps for two unrestraint dent cases of depths of 2.3% and 1.75% of the pipe diameter. These reported *h/D* ratios are measured after pressured rebounds from an initial indentation depth of *h/D* = 15%. The damage spreads within the shoulders of the dent on the outer surface of the pipe, leading to an axially oriented damage spot. This is a precursor for an axial fatigue crack within the dent region, as was experimentally [25] observed and highlighted in Figs. 44 and 45. Moreover, in shallow dents, the fatigue crack was indicated to be shifted closer to the center of the dent, as shown in Fig. 42b.

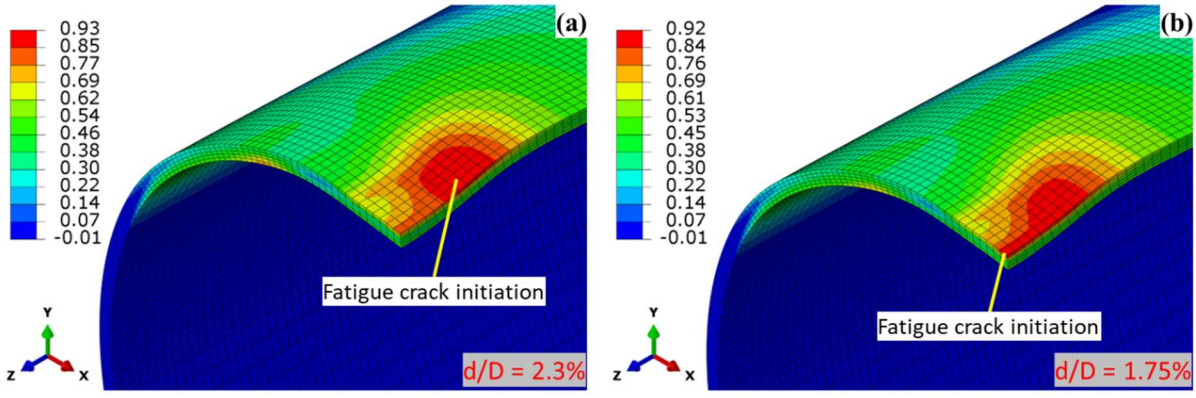

Figure 42: The progression of the total damage map of two unrestraint dent cases after the application of the fatigue loading: (a) a deep dent with a depth of 2.3% of the diameter of the pipe; (b) a shallow dent with a depth of 1.75% of the diameter of the pipe. The results in this figure are for the X70 steel pipe. Reported *h/D* ratios are the residual dent depth after pressure rebounds from initial indentation depth of *h/D* =15%.

For the restraint dent condition, fatigue cracks are biased to circumferentially initiated and propagated on the outer surface of the pipe, as shown in Fig. 43. More interestingly, the azimuthal position of the crack is modulated by the depth of the dent such that the crack becomes closer to the axial center of the pipe as the depth increases, as presented in Fig. 43a-c.

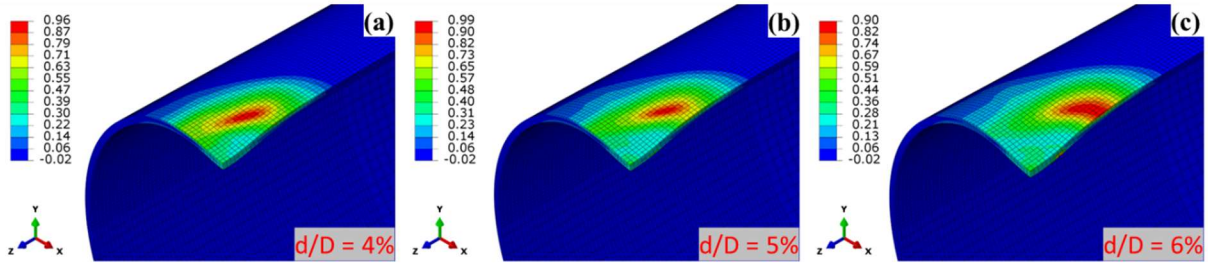

Figure 43: The progression of the total damage map of three shallow restraint dent cases after the application of the fatigue loading. (a) A dent with depth of 4.0% of pipe diameter. (b) A dent with depth of 5.0% of pipe diameter. (c) A dent with depth of 6.0% of the diameter of the pipe. The results in this figure are for the X70 steel pipe.

Sanjay et al. [25] performed a series of fatigue tests on restraint and unrestraint conditions for dents on X52 steel pipes. In their experiments, unrestraint dented pipe condition showed initiation of the fatigue cracks on the outer surface of the pipe and being oriented parallel to the axis of the pipe, as illustrated in Fig. 44a. In addition, fatigue cracks in the restraint cases were also initiated on the outer surface of the pipe with a circumferential orientation to the axis of the pipe, as shown in Fig. 44b. These experiment results agrees well with the damage patterns, shown in Fig. 43.

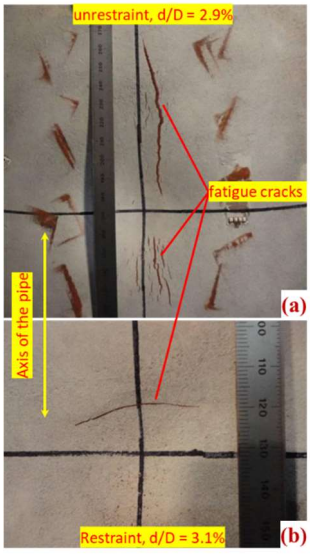

Figure 44: Photographs [25] of the experimental fatigue crack initiation of dented X52 steel pipes (OD = 457 mm and wall thickness is 7.9 mm). The center of the dent aligns with the crosshair marker on the pipe. (a) A residual unrestrained dent with (h/D = 2.9%). (b) A restrained dent (h/D = 3.1%).

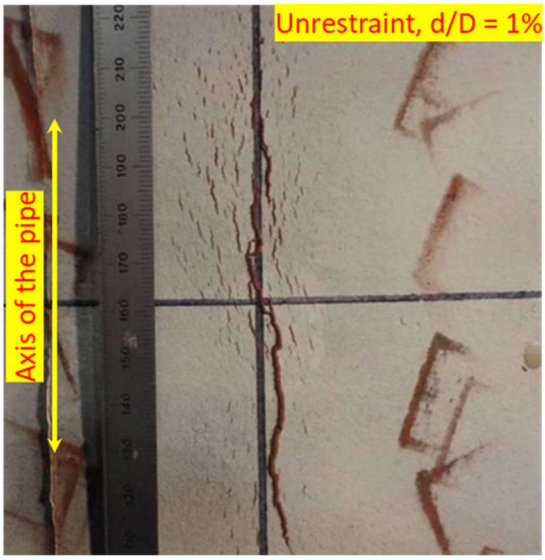

Figure 45: Photographs [25] of the experimental fatigue crack initiation of dented X52 steel pipes (OD = 457 mm and wall thickness is 7.9 mm). The center of the dent aligns with the crosshair marker on the pipe. A residual unrestrained dent with (h/D = 1.0%).

Moreover, as the dent becomes shallower, the fatigue crack was observed to be much closer to the center of the dent as compared to the deeper dents, as shown in Fig. 45. Such an observation confirms the predicted damage pattern, show in Fig. 42b. Similar to unrestraint case, the position, and the orientation of the fatigue cracks in restraint cases are influenced by the depth of the dent. In the case of shallow and unrestraint dents, fatigue cracks tend to initiate on the outer surface of the dent's shoulder, as shown in Fig. 43. As the dent depth increased, cracks were seen initiating on the inner surface of the pipe, as shown in Fig. 46a, b for two different dent depths of 7% and 11% of the diameter of the pipe, respectively. The shift of the crack from the outer surface to the inner surface is strongly believed to be related to the higher contact pressure underneath the indenter, such that the increased hydrostatic pressure increases the mean stress of the applied loading, which ultimately leads to a fast fatigue damage progression at the contact point between the pipe and the indenter, as shown in Fig. 46a (right). As the dent depth was further increased from 7% to 11% of the diameter of the pipe, the contact area between the pipe and the indenter was increased. Subsequently, the fatigue damage spanned over a larger area, compared to smaller depth, which led to a longer fatigue crack, as shown in Fig. 46b (right).

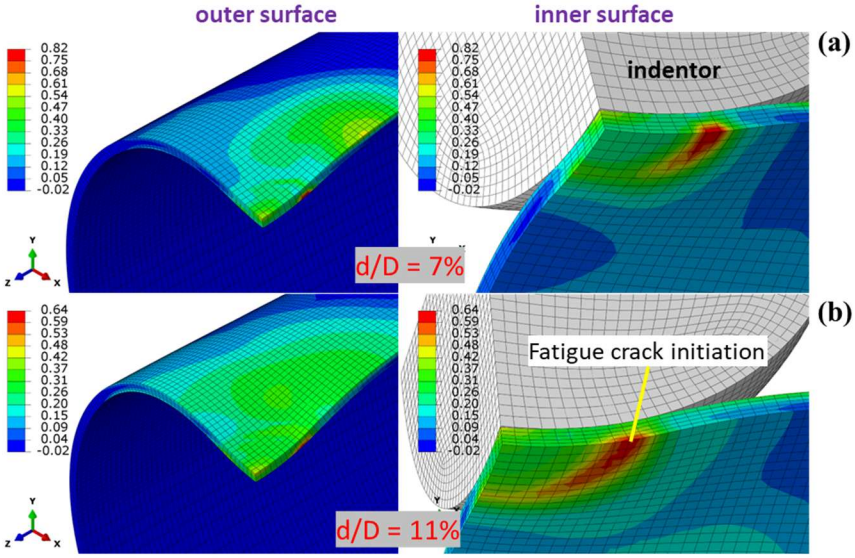

Figure 46: The progression of the total damage map of two deep restraint dent cases after the application of the fatigue loading: (a) a dent with a depth of 7.0% of the diameter of the pipe; (b) a dent with a depth of 11.0% of the diameter of the pipe. The damage on both the outer and inner surfaces of the pipe is shown on the left and the right sides, respectively. The results in this figure are for the X70 steel pipe.

Ultimately, the number of cycles to failure at a specific dent depth was computed while the accumulated damage reached 1 at some spatial location within the dented area. The location and pattern of the damage point to the initiation and propagation direction of potential fatigue cracks within the dented area of the pipe. Figure 47 summaries the computational estimates and experimental measurements [24] for the fatigue life of unrestraint dent condition at different dent depths for the examined X52 and X70 steel grades. In general, the model results fits well with the

experimental data. The added strength and toughness of X70 steel grade enables the alloy to sustain higher damage in the form of deeper indentation depth compared with the X52 grade, for the same fatigue life. To highlight the effect of restraint condition of the dented area, Fig. 48 shows about five times increase in the fatigue life compared to the unrestrained case for X70 steel grade. Again please note that for the unrestraint cases, the reported *h/D* ratios are the residual dent depth after pressure driven rebounding with different pressure levels from an initial indentation depth of *h/D* = 15%.

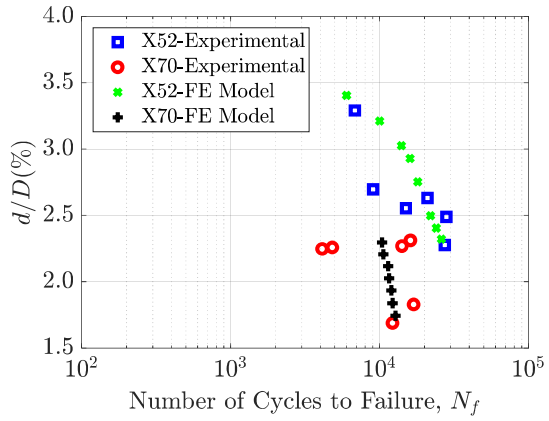

Figure 47: The fatigue life of unrestraint dent pipes of X52 and X70 steels with respect to the dent depth as a ratio of the outer diameter of the pipe obtained from the model and from the experimental work reported in [24].

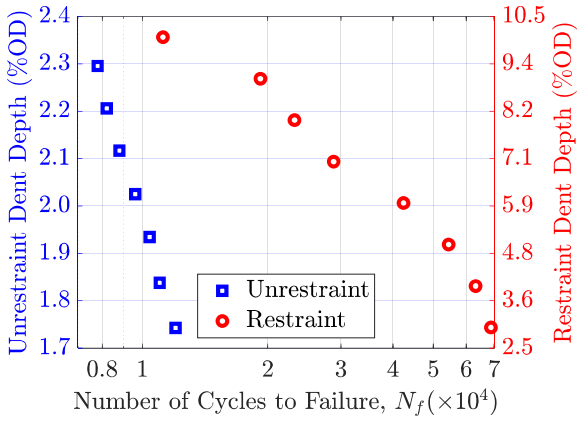

Figure 48: The fatigue life of restraint dent pipes of X70 steel with respect to the dent depth as a ratio of the outer diameter of the pipe obtained from the model.

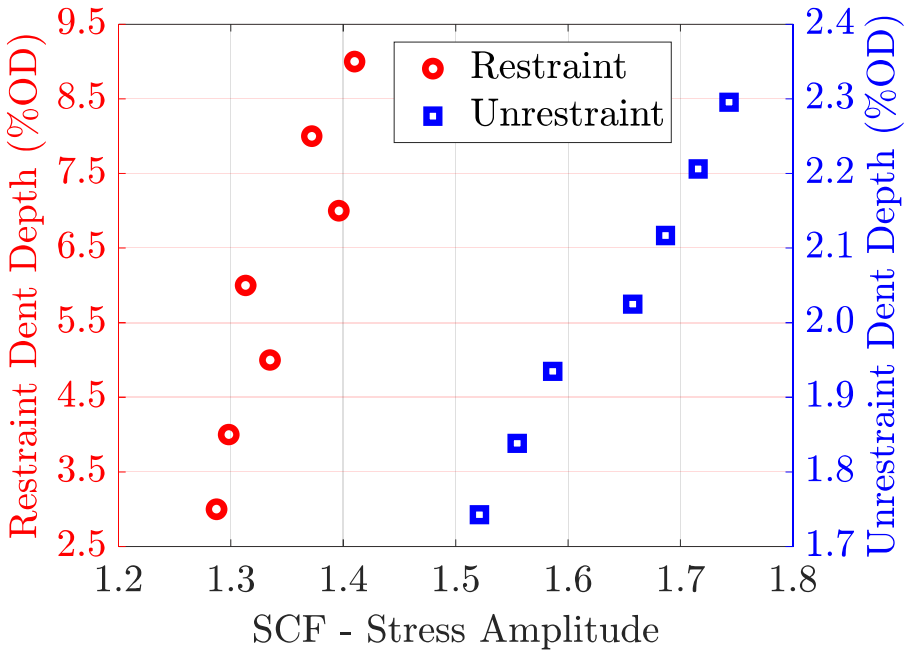

Figure 49: Model derived variation of stress concentration factor for the restraint and unrestraint dent conditions with respect to dent depth to pipe outer diameter ratio, measured at the peak of cyclic loading. For the unrestrained case, the noted depth is the residual depth after pressure driven rebound from an initial indentation depth ratio of *h/D* = 15%.

Such critical result of deterioration of the fatigue life arises from two contributing effects, (i) limitation on additional residual stresses and accumulated plastic strains arising the initial pressure rebounding, and (ii) restriction of the cyclic deformation under the restraint state if the indenter. To highlight the effect of such restriction on the characteristics of the cyclic loading and accumulated fatigue damage, Fig. 49 shows a measure of the cyclic stress concentration at the points of failure as a function of the indentation debt (*h/D* ratio). The shown stress concentration factor is the ratio of the effective stress amplitude at the critical failure point within the indentation area (i.e. at the inner or outer location within the indentation shoulder) to the remote effective stress amplitude away from dent area. Figure 49 clearly show that both the restraint and the unrestraint dent area will experience higher effective stress amplitude compared to a remote area from the dent. However, the unrestraint dent cases exhibited an increase in the stress concentration amplitude of about 20% compared to the restraint cases for the range of comparison of *h/D* ratios. The localized rise in effective stress amplitude within the dent area exacerbates the damage accumulation process and results in the observed reduction in the fatigue life.

D. Conclusion

In this study, we conducted a systematic analysis to investigate the influence of pre-existing plastic strain on the corrosion rate and remaining fatigue life of steel pipelines. This investigation involved electrochemical experiments conducted on pipeline specimens subjected to plastic deformation, alongside the development of a comprehensive numerical framework.

Electrochemical potentials were controlled to induce active dissolution in moderately alkaline carbonate-bicarbonate solutions, while the specimens were subjected to pre-accumulated plastic strains ranging from 0% to 4%. The electrochemical corrosion of X-70 steels resulted in stress corrosion cracking (IGSCC), characterized by penetration along the triple junctions and grain boundaries, ultimately leading to macroscopic crack formation. Triangular wedges were observed, their formation correlating with the level of accumulated plastic strains and the applied load profile. Electrochemical impedance spectroscopy (EIS) was employed to gain mechanistic and kinetic insights into the growth of corrosion product layers, particularly their concentration around grain boundary triple junctions. The resulting tensile stress ahead of the apex of these corrosion grooves acted as a driving force for crack formation. Although the applicability of EIS as a non-destructive evaluation (NDE) technique may be limited, its utilization in analyzing time-dependent corrosion product-induced stress, accounting for changes in groove shape and externally applied stresses, as well as plastic damage induced by dents, holds promise for developing a predictive framework for the initiation of stress corrosion cracking (SCC).

We have developed and implemented a continuum damage model as a user-material subroutine within the ABAQUS finite element package. This model offers a cohesive integration of various damage mechanisms, encompassing initial plastic damage resulting from dents or gouges, corrosion-induced damage, and elasto-plastic damage induced by fatigue. The framework is

founded upon the damage-coupled elastoplastic fatigue model pioneered by LeMaitre and Chaboche. The dent deformation and subsequent rebound cycle, if permitted, facilitate the assessment of initial plastic strain damage. Subsequently, the elasto-plastic fatigue module tracks the accumulation of damage. The failure criterion is defined by reaching a critical damage value (D=1), corresponding to the initiation of macro-cracks after a certain number of fatigue cycles. While corrosion is exacerbated by the residual plastic strain stemming from gouges and dents, further work is required to provide a quantitative description of this phenomenon.

The continuum damage model has been calibrated using full-scale fatigue test datasets for X52 and X70 grade pipeline steels. The model's predictions align closely with the full-scale test results, demonstrating accurate estimation of life to failure, spatial localization of failure near the dented section, and their evolution with increasing dent depth/pipe diameter ratio. Furthermore, the modeling framework exhibits discernible characteristics regarding fatigue crack initiation under both restrained and unrestrained dented pipe conditions. It is observed that in the case of an unrestrained dent, additional stress concentration is geometrically imposed, proportional to the initial dent depth. This additional stress concentration may escalate to as much as 20% of the levels expected under normal operating pressure. Such heightened stress amplitudes significantly accelerate fatigue life deterioration compared to the restrained case.

The experimentally validated computational framework is well-suited for systematic examination of multi-threat analysis at the structural scale.

E. References

1. Lemaitre, J., & Chaboche, J. L. (1994). Mechanics of solid materials. Cambridge university press.
2. Lemaitre, J., & Desmorat, R. (2006). Engineering damage mechanics: ductile, creep, fatigue and brittle failures. Springer Science & Business Media.
3. Wu, H. C. (2004). Continuum mechanics and plasticity. Chapman and Hall/CRC.
4. Dunne, F., & Petrinic, N. (2005). Introduction to computational plasticity. OUP Oxford.
5. Prager, W.: A new method of analyzing stresses and strains in work hardening plastic solids. J. Appl. Mech. 23, 795–810 (1956)
6. Lubliner, J. (2008). Plasticity theory. Courier Corporation.
7. Simo, J. C., & Hughes, T. J. (2006). Computational inelasticity (Vol. 7). Springer Science & Business Media.
8. Armstrong, P. J., & Frederick, C. O. (1966). A mathematical representation of the multiaxial Bauschinger effect (Vol. 731). Berkeley, CA: Berkeley Nuclear Laboratories.
9. Chaboche, J.L., Rousselier, G.: On the plastic and viscoplastic constitutive equations - part II: application of internal variable concepts to the 316 stainless steel. J. Press. Vessel Technol. 105, 159–164 (1983)
10. Voce, E.: The relationship between stress and strain for homogeneous deformation. J. Inst. Metals 74, 537–562 (1948)
11. Lemaitre J. Formulation and identification of damage kinetic constitutive equations. In: Krajcinovic D, Lemaitre J, editors. Continuum damage mechanics: theory and applications. CISM courses and lectures no. 295. Wien: Springer; 1987. p. 37–99.
12. Suchocki, C. (2022). On finite element implementation of cyclic elastoplasticity: theory, coding, and exemplary problems. Acta Mechanica, 233(1), 83-120.
13. Kang, G., Liu, Y., Ding, J., & Gao, Q. (2009). Uniaxial ratcheting and fatigue failure of tempered 42CrMo steel: Damage evolution and damage-coupled visco-plastic constitutive model. International journal of Plasticity, 25(5), 838-860.
14. Chaboche, J. L., & Lesne, P. M. (1988). A nonlinear continuous fatigue damage model. Fatigue & fracture of engineering materials & structures, 11(1), 1-17.
15. Sines, G. (1959). Behavior of metals under complex static and alternating stresses. Metal fatigue, 1, 145-169.
16. Zhang, T., McHugh, P. E., & Leen, S. B. (2012). Finite element implementation of multiaxial continuum damage mechanics %for plain and fretting fatigue. International Journal of Fatigue, 44, 260-272.
17. Liu, N., Cui, X., Xiao, J., Lua, J., & Phan, N. (2020). A simplified continuum damage mechanics based modeling strategy for cumulative fatigue damage assessment of metallic bolted joints. International Journal of Fatigue, 131, 105302.
18. https://www.astm.org/e0466-21.html
19. Military Handbook – MIL-HDBK-5H: Metallic materials and elements for aerospace vehicle structures (Knovel interactive ed.). US Department of Defense; 1998.

20. Lefranc, P., Doquet, V., Gerland, M., & Sarrazin-Baudoux, C. (2008). Nucleation of cracks from shear-induced cavities in an α/β titanium alloy in fatigue, room-temperature creep and dwell-fatigue. Acta Materialia, 56(16), 4450-4457.
21. Al-Rubaie, K. S., Del Grande, M. A., Travessa, D. N., & Cardoso, K. R. (2007). Effect of pre-strain on the fatigue life of 7050-T7451 aluminium alloy. Materials Science and Engineering: A, 464(1-2), 141-150.
22. Silitonga, S., Maljaars, J., Soetens, F., & Snijder, H. H. (2013). Survey on damage mechanics models for fatigue life prediction. Heron, 58(1), 25-60.
23. Zhan, Z., Hu, W., Li, B., Zhang, Y., Meng, Q., & Guan, Z. (2017). Continuum damage mechanics combined with the extended finite element method for the total life prediction of a metallic component. International Journal of Mechanical Sciences, 124, 48-58.
24. Bolton, B., Semiga, V., Tiku, S., Dinovitzer, A., & Zhou, J. (2010, January). Full scale cyclic fatigue testing of dented Pipelines and development of a Validated Dented Pipe Finite Element Model. In International Pipeline Conference (Vol. 44205, pp. 863-872).
25. Tiku, S., Semiga, V., Dinovitzer, A., & Vignal, G. (2012, September). Full scale cyclic fatigue testing of dented Pipelines and development of a Validated Dented Pipe Finite Element Model. In International Pipeline Conference (Vol. 45134, pp. 693-702). American Society of Mechanical Engineers.
26. Md Liakat Ali, Degradation and Fatigue Involving Dissipated Processes, PhD Thesis, Louisiana State University 2015.
27. Tian, P., Xu, K., Lu, G. P., Qiao, G. Y., Liao, B., & Xiao, F. R. (2018). Evaluation of the mechanical properties of the X52 high frequency electric resistance welding pipes. International Journal of Pressure Vessels and Piping, 165, 59-67.
28. Turhan, Ş. Ö., Motameni, A., & Gürbüz, R. (2020). Fatigue behavior of welded API 5L X70 steel used in pipelines. Journal of Failure Analysis and Prevention, 20, 1554-1567.
29. Gajdos, L'ubomir, Sperl, M., & Bystriansky, J. (2015). Fatigue behaviour of X70 steel in crude oil. MATERIALI IN TEHNOLOGIJE, 49(2), 243-246.
30. Fernandes, A. A., de Jesus, A. M., & Jorge, R. N. (Eds.). (2018). Monotonic and Ultra-Low-Cycle Fatigue Behaviour of Pipeline Steels: Experimental and Numerical Approaches. Springer.
31. Ouladbrahim, A., Belaidi, I., Khatir, S., Magagnini, E., Capozucca, R., & Wahab, M. A. (2022). Prediction of Gurson damage model parameters coupled with hardening law identification of Steel X70 pipeline using neural network. Metals and Materials International, 28(2), 370-384.
32. Xi, G., Lei, J., Qiu, J., Ma, Y., & Yang, R. (2020). A semi-quantitative explanation of the cold dwell effect in titanium alloys. Materials & Design, 194, 108909.
33. Jelen, D., Tiku, S., Eshraghi, A., John, B., Dinovitzer, A., Zarea, M., ... & Bertin, M. (2017). Full Scale Testing of Interactive Features for Improved Models. Final Report, DTPH56-14-H00002. https://primis.phmsa.dot.gov/matrix/FilGet.rdm?fil=11764.
34. F. Farelas, M. Galicia, B. Brown, S. Nesic, H. Castaneda (2010). Evolution of dissolution processes at the interface of carbon steel corroding in a CO2 environment studied by EIS.

Corrosion Sci., 52, 509-517.
35. P. Mishra, D. Yavas, A.F. Bastawros, K.R. Hebert (2020). Electrochemical impedance spectroscopy analysis of corrosion product layer formation on pipeline steel. Electrochimica Acta 346, 136232.
36. J. Newman, K.E. Tomas-Alyea (2004). Electrochemical Systems. Wiley, Chichester, UK.
37. R.E. Zeebe (2011). On the molecular diffusion coefficients of dissolved CO_2, HCO_3^-, and CO_3^{2-} and their dependence on isotopic mass Geochem. Cosmochim. Acta, 75, 2483-2498.
38. C.R. Wilke, M. Eisenberg, C.W. Tobias (1953). Correlation of limiting currents under free convection conditions. J. Electrochem. Soc., 100, 513-523.
39. D. Yavas, A. Alshehri, P. Mishra, P. Shrotriya, A.E. Bastawros, K.R. Hebert (2018). Morphology and stress evolution during the initial stages of intergranular corrosion of X70 steel. Electrochim. Acta, 285, 336-343.
40. D. McNaughtan, M. Worsfold, M.J. Robinson (2003). Corrosion product force measurements in the study of exfoliation and stress corrosion cracking in high strength aluminium alloys. Corrosion Sci., 45, 2377-2389.
41. H. Gao, L. Zhang, W.D. Nix, C.V. Thompson, E. Arzt (1999). Crack-like grain-boundary diffusion wedges in thin metal films. Acta Mater., 47, 2865-2878.
42. E. Wendler-Kalsch (1980). The effects of film formation and mechanical factors on the initiation of stress corrosion cracking of unalloyed steels in carbonate solutions. Werkstoffe Korrosion, 31, 531-542.
43. R.N. Parkins, S. Zhou (1997). The stress corrosion cracking of C-Mn Steel in CO_2-HCO_3^--CO_3^{2-} solutions. II. Electrochemical and other data. Corrosion Sci., 39, 175-191.